

1 **Utilization of O₄ slant column density to derive aerosol layer height**
2 **from a spaceborne UV-Visible hyperspectral sensor: Sensitivity and**
3 **case study**

4

5 Sang Seo Park^{1,+}, Jhoon Kim^{1,*}, Hanlim Lee^{1,2}, Omar Torres³, Kwang-Mog Lee⁴, Sang
6 Deok Lee⁵

7 ¹Department of Atmospheric Sciences, Yonsei University, Seoul, Korea.

8 ²Department of Spatial Information Engineering, Pukyong National University, Busan,
9 Korea

10 ³NASA Goddard Space Flight Center, Greenbelt, Maryland, United States

11 ⁴Department of Astronomy and Atmospheric Science, Kyungpook National University,
12 Daegu, Korea

13 ⁵National Institute of Environment Research, Ministry of Environment, Incheon, Korea

14 ⁺Now at Research Institute of Applied Mechanics, Kyushu University, Fukuoka, Japan

15

16 * Correspondence to: Jhoon Kim (jkim2@yonsei.ac.kr)

17 Tel. : +82-2-2123-5682, Fax: +82-2-365-5163

18

Abstract

The sensitivities of oxygen-dimer (O_4) slant column densities (SCDs) to changes in aerosol layer height are investigated using the simulated radiances by a radiative transfer model, the Linearized pseudo-spherical vector discrete ordinate radiative transfer (VLIDORT), and the Differential Optical Absorption Spectroscopy (DOAS) technique. The sensitivities of the O_4 index (O_4I), which is defined as dividing O_4 SCD by 10^{40} molecules²cm⁻⁵, to aerosol types and optical properties are also evaluated and compared. Among the O_4 absorption bands at 340, 360, 380, and 477 nm, the O_4 absorption band at 477 nm is found to be the most suitable to retrieve the aerosol effective height. However, the O_4I at 477 nm is significantly influenced not only by the aerosol layer effective height but also by aerosol vertical profiles, optical properties including single scattering albedo (SSA), aerosol optical depth (AOD), particle size, and surface albedo. Overall, the error of the retrieved aerosol effective height is estimated to be 1276, 846, and 739 m for dust, non-absorbing, and absorbing aerosol, respectively, assuming knowledge on the aerosol vertical distribution shape. Using radiance data from the Ozone Monitoring Instrument (OMI), a new algorithm is developed to derive the aerosol effective height over East Asia after the determination of the aerosol type and AOD from the MODerate resolution Imaging Spectroradiometer (MODIS). About 80% of retrieved aerosol effective heights are within the error range of 1 km compared to those obtained from the Cloud-Aerosol Lidar with Orthogonal Polarization (CALIOP) measurements on thick aerosol layer cases.

42 1. Introduction

43 Aerosol is one of the key atmospheric constituents in understanding climate
44 changes with its effects on direct and diffuse solar radiation (e.g., Haywood and Shine,
45 1995; Kaufman *et al.*, 2002), and plays an important role in air quality near the surface
46 (e.g., Watson *et al.*, 1994; Prospero, 1999). For these reasons, observations from
47 satellite remote sensing have been carried out to investigate aerosol properties at
48 regional and global scale, including aerosol optical depth (AOD) (e.g., Currier *et al.*,
49 2008; Levy *et al.*, 2007; Torres *et al.*, 2007; Ahn *et al.*, 2014; Veefkind *et al.*, 1999;
50 Zhang *et al.*, 2011), fine mode fraction (FMF) or Angstrom Exponent (AE) (e.g., Jones
51 and Christopher, 2007; Lee *et al.*, 2010; Nakajima and Higurashi, 1998; Remer *et al.*,
52 2008), single scattering albedo (SSA) (e.g., Dubovik *et al.*, 2002; Levy *et al.*, 2007;
53 Jeong and Hsu, 2008; Torres *et al.*, 1998, 2005, 2007; Jethva *et al.*, 2014), and aerosol
54 types (e.g., Higurashi and Nakajima, 2002; Kim *et al.*, 2007; Lee *et al.*, 2010). These
55 information were further utilized to estimate radiative forcing of aerosol (e.g.,
56 Christopher *et al.*, 2006; Chung *et al.*, 2005; Chou *et al.*, 2002), to understand the
57 mechanism of the changes to the cloud formation (Twomey *et al.*, 1984; Albrecht,
58 1989; Jones *et al.*, 1994), and to monitor air quality (e.g., Wang and Christopher, 2003;
59 Hutchison *et al.*, 2005).

60 Vertical profiles of atmospheric aerosols are affected by processes of formation,
61 transport and deposition, and vary for different aerosol types over East Asia (Shimizu
62 *et al.*, 2004). Labonne *et al.* (2007) also reported that the layer top height of biomass
63 burning aerosol ranged from 1.5 to 7 km in the wild fire regions. The information on
64 the aerosol layer height is important, because the variation of the aerosol vertical
65 distribution affects radiative process in the atmosphere near the surface and trace gas

66 retrieval for air mass factor calculation. Uncertainty in aerosol layer height also affects
67 the accuracy of AOD and SSA retrieval algorithms that use near UV observations
68 (Torres *et al.*, 1998; Torres *et al.*, 2007; Jethva *et al.*, 2014) and complicates the
69 interpretation of the Aerosol Index (AI), a qualitative parameter commonly used to
70 detect absorbing aerosols (Herman *et al.*, 1997; Torres *et al.*, 1998). In addition, there
71 have been difficulties to estimate surface concentration of aerosol from AODs, because
72 the information on aerosol vertical distribution is not readily available and even hard to
73 predict from the state-of-the-art models due to its large variability. Although the Cloud-
74 Aerosol Lidar with Orthogonal Polarization (CALIOP) has been successful and
75 provided vertical profiles of aerosols, its spatial coverage was very limited with its
76 measurement characteristics (Omar *et al.*, 2009). Liu *et al.* (2005) showed that the
77 Particulate Matter (PM) concentration estimated by the AOD from satellite observation
78 accounted for only 48% of the measured surface PM, although their study reflected
79 variations of the aerosol types and its hygroscopic growth in the algorithms. One of the
80 essential factors to consider in estimating PM from AOD is the vertical structure of
81 aerosols (e.g. Chu, 2006; Seo *et al.*, 2015). Therefore, conventional aerosol products
82 would benefit significantly with the development of robust algorithm to retrieve
83 aerosol height using satellite data.

84 The Differential Optical Absorption Spectroscopy (DOAS) technique has been
85 used widely to retrieve trace gas concentration both from ground-based (e.g., Platt,
86 1994; Platt and Stutz, 2008) and space-borne (e.g., Wagner *et al.*, 2007; Wagner *et al.*,
87 2010) measurements. After the work of Platt (1994) to retrieve trace gas concentration
88 by using DOAS, Wagner *et al.* (2004) suggested to derive atmospheric aerosol
89 information from O₄ measurement by using Multi Axis Differential Optical Absorption

90 Spectroscopy (MAX-DOAS). Friess *et al.* (2006) analyzed the model studies to
91 calculate the achievable precision of the aerosol optical depth and vertical profile. In
92 addition, several studies (e.g., Irie *et al.*, 2009 and 2011; Lee *et al.*, 2009 and 2011;
93 Clemer *et al.*, 2010; Li *et al.*, 2010) provided aerosol profiles from ground-based
94 hyperspectral measurements in UV and visible wavelength ranges on several ground
95 sites. Wagner *et al.* (2010) investigated the sensitivity of various factors to the aerosol
96 layer height using the data obtained from the SCanning Imaging Absorption
97 SpectroMeter for Atmospheric ChartographY (SCIAMACHY) on ENVISAT. The
98 sensitivity of the Ring effect and the absorption by oxygen molecule (O₂) and its dimer
99 (O₄) calculated by DOAS method were examined to estimate aerosol properties
100 including the layer height. Kokhanovsky and Rozanov (2010) estimated dust altitudes
101 using the O₂-A band between 760 and 765 nm after the determination of the dust
102 optical depth. In addition, several previous studies are also investigated estimation
103 methods for aerosol height information by using hyperspectral measurement in visible
104 (e.g., Dubuisson *et al.*, 2009; Koppers and Murtagh, 1997; Sanders and de Haan, 2013;
105 Sanghavi *et al.*, 2012; Wang *et al.*, 2012). Because the surface signal is significantly
106 smaller than the aerosol signal in the near UV, these wavelength regions are useful to
107 derive aerosol height information from space borne measurements.

108 For OMI measurement, the O₄ band at 477 nm has been widely applied to
109 estimate cloud information (e.g., Accarreta *et al.*, 2004; Sneepe *et al.*, 2008). Especially,
110 the cloud information retrieved by O₄ band at 477 nm was used to analyze air mass
111 factor (AMF) with the consideration of aerosol optical effects for the NO₂ column
112 retrieval (e.g., Castellanos *et al.*, 2015, Chimot *et al.*, 2015; Lin *et al.*, 2014; Lin *et al.*,
113 2015). Although O₄ absorption band around 477 nm varies also due to cloud existence,

114 it can be also used for the aerosol optical parameter estimation. Veihelmann *et al.*
115 (2007) introduced that the 477 nm channel, a major O₄ band, significantly adds degree
116 of freedom for aerosol retrieval by using principal component analysis, and Dirksen *et*
117 *al.* (2009) adopts the pressure information obtained from OMI O₄ band to identify a
118 plume height for aerosol transport cases.

119 In this study, the sensitivities of the O₄ bands at 340, 360, 380, and 477 nm to
120 changes in aerosol layer height and its optical properties are estimated using simulated
121 hyperspectral radiances, differently from the previous studies using the O₂-A band
122 observation (e.g., Kokhanovsky and Rozanov, 2010). We proposed an improved DOAS
123 algorithm for the O₄ absorption bands to retrieve aerosol height information from the
124 O₄ slant column densities (SCDs) based on the sensitivity studies. This new algorithm
125 is applied to the O₄ SCD from the Ozone Monitoring Instrument (OMI) to retrieve the
126 aerosol effective height (AEH) for a real case over East Asia, including error estimates.

127

128 **2. Methods**

129 In general, scattering by aerosol at low altitudes leads to an increase in the length
130 of the average light path (enhancement effect), while those at high altitudes causes a
131 decrease in the length of the average light path (shielding effect) (Wagner *et al.*, 2010).
132 These two opposing effects change the estimated O₄ SCD values. Furthermore, the
133 measured O₄ SCD is a function of wavelength, because the absorption and scattering
134 by atmospheric molecules and aerosols have spectral dependence. Therefore, radiative
135 transfer calculations are carried out to estimate the sensitivity of the O₄ SCD with
136 respect to the change of atmospheric conditions. Details of the radiative transfer model
137 (RTM) and input parameters to simulate radiance are discussed in section 2.1.

138 Analytical method of the DOAS to estimate the O₄ is described in section 2.2.

139

140 **2.1. Simulation of hyperspectral radiance**

141 Figure 1 shows the flowchart of the method to estimate the O₄ SCD from the
142 simulated radiance. Because the magnitude of the O₄ SCD values is too large to
143 express the sensitivity results, this paper defines the O₄ index (O4I) which divides O₄
144 SCD by 10⁴⁰ molecules²cm⁻⁵. In order to investigate the sensitivities of the O4I at
145 several bands in UV and visible wavelengths with respect to various aerosol properties,
146 including AEHs, aerosol amounts and aerosol types, the hyperspectral radiance is
147 simulated using the Linearized pseudo-spherical vector discrete ordinate radiative
148 transfer (VLIDORT) model (Spurr, 2006). The VLIDORT model is based on the
149 linearized discrete ordinate radiative transfer model (LIDORT) (Spurr *et al.*, 2001;
150 Spurr, 2002). This RTM is suitable for the off-nadir satellite viewing geometry of
151 passive sensors since this model adopts the spherically curved atmosphere to reflect
152 the pseudo-spherical direct-beam attenuation effect (Spurr *et al.*, 2001). The model
153 calculates the monochromatic radiance ranging from 300 to 500 nm with a spectral
154 resolution of 0.1 nm. The radiance spectrum is calculated with a 0.2 nm sampling
155 resolution applying a slit response function (SRF) given by a normalized Gaussian
156 distribution with 0.6 nm as the full-width half maximum (FWHM).

157

158 **2.1.1. Aerosol properties**

159 The aerosol input parameters for the RTM are important in simulating the
160 radiance spectra because aerosol optical properties determine scattering and absorption
161 characteristics. The data from the Optical Properties of Aerosol and Cloud (OPAC)

162 package (Hess *et al.*, 1998) are used as aerosol parameters, which includes the spectral
163 complex refractive indices and size distribution of aerosols, to calculate SSA and phase
164 function through the Mie calculations. The information of the aerosol parameters is not
165 available at the UV wavelengths, since the AERONET observation provides the
166 information of those aerosol parameters in the visible.

167 In terms of the aerosol types, water soluble (WASO), mineral dust (MITR), and
168 continental polluted (COPO) model are selected to simulate non-absorbing aerosol,
169 mineral dust, and absorbing anthropogenic aerosol, respectively. The COPO is
170 combined type including both soot and WASO, which represents the pure black-carbon
171 and non-absorbing aerosols, respectively. The mixture of these two types, adequately
172 describes the fine mode aerosol from anthropogenic pollution. The SSA is the largest
173 for WASO and the smallest for COPO. In order to account for hygroscopic growth, the
174 default relative humidity is assumed to be 80 % (c.f., Holzer-Popp and Schroedter-
175 Homscheidt, 2004).

176

177 **2.1.2. Aerosol vertical distribution**

178 In this present study, ‘aerosol height’ refers to aerosol effective height (AEH),
179 defined as the peak height in Gaussian distribution. According to Hayasaka *et al.*
180 (2007), however, the aerosol extinction coefficient was found to exponentially
181 decrease with altitude over East Asia based on the ground-based LIDAR observation
182 data during the Atmospheric Brown Clouds-East Asia Regional Experiment 2005
183 (ABC-EAREX 2005) campaign. Previous studies used the exponentially decreasing
184 pattern with altitude to represent the aerosol vertical profiles (e.g. Hayasaka *et al.*,
185 2007; Li *et al.*, 2010), and reported that aerosol is present within 5 km in altitude for

186 most of the cases (e.g. Sasano, 1996; Chiang *et al.*, 2007). On the other hands, the
187 aerosol vertical distribution does not always follow exponential profile. For the long-
188 range transported aerosol such as dust cases, the aerosol layer profile is quite different
189 than exponential profile and occasionally transported to well above the boundary layer
190 (e.g., Reid *et al.*, 2002; Johnson *et al.*, 2008). The peak height of aerosol extinction
191 profile in long-range transport cases was reported to be located between 1 and 3 km
192 during the Dust and Biomass-burning Aerosol Experiment (DABEX) campaign
193 (Johnson *et al.*, 2008). From these previous studies, standard aerosol vertical profile is
194 difficult to determine. For algorithm development, previous studies assumed that the
195 vertical distribution is Gaussian function defined by peak height and half width as
196 representative parameters (Torres *et al.*, 1998; Torres *et al.*, 2005). To supplement the
197 simplicity of assumption for aerosol vertical distribution, aerosol vertical distributions
198 are assumed to be quasi-Gaussian generalized distribution function (GDF), which is
199 Gaussian distribution with dependence on aerosol peak height, width, and layer top
200 and bottom height. Details of GDF can be found in Spurr and Christi (2014) and Yang
201 *et al.* (2010). In this study, AEH ranges from 1 to 5 km with 1 km width as 1-sigma for
202 the RTM simulation.

203

204 **2.1.3. Atmospheric gases**

205 The vertical distribution of the O₄ number density, which is used to calculate its
206 SCD from the RTM, is assumed to be the square of the O₂ number density in each
207 layer (Hermans *et al.*, 2003). Thus, the total number of the O₄ column density from
208 surface to TOA is 1.38×10^{43} molecule²cm⁻⁵, where 93% and 73% of the total O₄ is
209 distributed below the altitude of 10 km and 5 km, respectively. In particular, signals by

210 the changes of O₄ are strong below 5 km, where aerosol transports are observed
211 frequently. The vertical distributions of other atmospheric components are taken from
212 the US standard atmosphere 1976 (United States Committee on Extension to the
213 Standard Atmosphere, 1976). The vertical distribution of trace gases and aerosol in the
214 troposphere are interpolated in the 0.1 km resolution from the sea level to 5 km.

215

216 **2.2. DOAS analysis for O₄I estimation**

217 Table 1 summarizes the absorption cross sections of trace gases used as inputs for
218 the radiance simulations and the DOAS spectral analysis. At wavelengths of 340, 360,
219 380, and 477 nm, the O₄ absorption cross section from Hermans *et al.* (1999) is used in
220 this study. O₃ absorption cross sections at three different temperatures (223, 243, and
221 273 K) and NO₂ absorption cross sections at two different temperatures (220 and 294
222 K) are used to account for the amounts in the stratosphere and the troposphere. The
223 radiance information obtained from the RTM simulation is analyzed to derive the O₄
224 SCDs using WinDOAS software (van Roozendael and Fayt, 2001) before O₄I
225 estimation. To analyze the simulated radiances, the spectrum calculated without all
226 atmospheric gases and aerosol are used as the Fraunhofer reference spectrum (FRS).
227 The simulated spectra are fitted simultaneously with the absorption cross sections of
228 all trace gases listed in Table 1 and FRS in the respective wavelength range of 335-350,
229 350-370, 370-390, and 460-486 nm, using a nonlinear least squares method (Platt and
230 Stutz, 2008).

231 On the other hand, the O₄I from OMI standard product of cloud (OMCLDO2)
232 (e.g., Accarreta *et al.*, 2004; Sneep *et al.*, 2008) is used to adopt the AEH retrieval for
233 case study. The OMCLDO2 basically used the cross section database from Newnham

234 and Ballard (1998) considering the temperature dependence by interpolating to
235 representative atmospheric temperature of 253 K (Accarreta *et al.*, 2004). For this
236 reason, there can be systematic difference between the O₄I from OMCLDO2 and
237 direct estimation from the observed radiance spectra in this present study. Figure 2
238 shows the O₄ SCD from OMCLDO2 and those directly retrieved from radiance
239 spectrum over all observed OMI pixels on March 31, 2007 over East Asia. Similar to
240 the DOAS analysis using the simulated spectra for a look-up table (LUT) calculation,
241 OMI observed radiance spectra are fitted with the Ring spectrum and the FRS in
242 addition to the absorption cross sections in Table 1 within the same wavelength
243 window. Before the spectral fitting, the NO₂ and O₃ cross sections are I_0 corrected, and
244 the Ring spectrum (Fish and Jones, 1995), accounting for the effects of the rotational
245 Raman scattering due to air molecules, is calculated using the WinDOAS software
246 (van Roozendael and Fayt, 2001). After the fitting, the noise level of residual spectrum
247 is estimated to be on the order of 10^{-3} for the radiance spectrum at 477 nm from OMI
248 measurements. The O₄ SCDs with the fitting error less than 1% is used for the
249 comparison. From this figure, a systematic difference between the two different fitting
250 results is less than 1%, although the cross section databases for fitting are different.
251 From this result, the effect of cross section database difference is negligible when the
252 same observation data was used. Furthermore, the DOAS analysis for LUT calculation
253 can be used to compare the O₄ SCD from OMCLDO2.

254 Figure 3 shows the comparison of the O₄ SCD at 477 nm from LUT with the
255 dimension as in Table 2 against OMCLDO2 for aerosol and cloud free pixels in year
256 2005. The LUT of O₄ SCD is estimated by the DOAS analysis using simulated
257 radiance from VLIDORT with various geometries as shown in Table 2. The clear sky

258 region is selected for the Pacific Ocean with cloud fraction less than 0.02 from OMI
259 observation. The surface albedo is assumed to be 0.05, which is similar to the
260 minimum Lambertian equivalent reflectance (LER) over clear ocean surface (e.g.,
261 Kleipool *et al.*, 2008). Because the standard product of the O₄ SCD is only estimated at
262 the 477 nm band, the results can be compared only at this band. To minimize the
263 DOAS fitting error, the observed data from OMI is selected by the fitting precision less
264 than 2% and the quality flags for spectral fitting are also considered. As shown in
265 Figure 3(a), the coefficient of determination (R^2) is 0.864 with a slope of 1.050, and
266 the LUT exhibits a ratio of 0.86 ± 0.05 to the values obtained from OMI standard values.
267 Despite the statistically significant R^2 and slope values between the two values, there
268 exists negative bias by about 14%.

269 The bias between the retrieved from LUT and the estimated from standard
270 product values can be attributed to the differences in the O₄ cross section data and the
271 lack of their temperature and pressure dependence as noted from the previous works by
272 Wagner *et al.* (2009), Clemer *et al.* (2010), and Irie *et al.* (2015). For this reason,
273 ground-based measurements adopted the correction factors to cross section database.
274 However the bias effect for the cross section difference is limited as shown in Figure 2,
275 and the correction factor for the cross section database in the previous studies cannot
276 be adopted to the space-borne measurements. From Kleipool *et al.* (2008), the
277 minimum LER is defined to be the 1% cumulative probability threshold, and frequent
278 LER value are typically higher than minimum LER over clear ocean, although cloud
279 screening was perfectly executed before LER calculation. To account for the difference
280 between simulated and observed SCD, the LUT was re-calculated by changing
281 condition to the surface albedo of 0.10. Although assumed surface albedo is higher

282 than minimum LER from Kleipool *et al.* (2008), the surface albedo of 0.10 is realistic
283 value for ocean surface albedo at mid-latitude (e.g., Payne, 1972). The corrected result
284 is shown in Figure 3(b), with the R^2 of 0.865 similar to that before the correction,
285 while the negative bias is removed to 0.98 ± 0.05 and the regression line slope is 1.123.
286 Although the comparison result is not perfect, the calculation by the VLIDORT
287 simulates the satellite observation and can be used for sensitivity tests and case studies
288 to retrieve aerosol height.

289

290 **3. Sensitivity test**

291 **3.1. Sensitivity of the O4Is to the AEH**

292 The sensitivity of the O4I to the AEH is investigated for its absorption bands at
293 340, 360, 380, and 477 nm. Figure 4 shows the O4I as a function of the AEH and the
294 three different aerosol types of MITR, WASO and COPO at 360, 380, and 477 nm,
295 respectively. The vertical error bar represents the fitting error estimated by the residual
296 spectra from the DOAS fitting (e.g., Stutz and Platt, 1996). For the calculation shown
297 in the figures, the following geometries are assumed: solar zenith angle (SZA) of 30
298 degrees, viewing zenith angle (VZA) of 30 degrees, and relative azimuth angle (RAA)
299 of 100 degrees. Note that insignificant SCD value was estimated at 340 nm due to the
300 large spectra fitting error. In these three figures, the O4Is show the AEHs ranging from
301 1.0 to 5.0 km for the AODs of 1.0 and 2.5 at 500 nm, which could be due to the
302 existence of thick aerosol layers. For the sensitivity result, the decrease rate of the O4I
303 value in the 1 km interval of AEH ($-dO_4/dZ$) is defined as equivalent O4I difference
304 converting from O4I difference between neighbor AEH in same AOD condition.

305 The O4Is are estimated at 360 and 380 nm band as shown in Figure 4(a) ~ (f).

306 The O4I is significantly decreased with increasing AEH at 360 and 380 nm for all
307 aerosol types. However negative O4Is are occasionally estimated at 360 nm.
308 Furthermore the fitting errors are too large to estimate the AEH, which range from 160
309 to 410 at 360 nm and from 350 to 1060 at 380 nm. From large fitting error with small
310 O4I, the fitting results are insignificant at these two absorption bands.

311 On the other hand, the sensitivity of the O4I at 477 nm is a significant variable to
312 estimate AEH. The mean value of $-dO_4/dZ$ is estimated to be 87, 290, and 190 for the
313 MITR, WASO, and COPO when the AOD is 1.0, respectively. The mean value of $-$
314 dO_4/dZ on the AOD of 2.5 is estimated to be 94, 362, and 213 for the MITR, WASO,
315 and COPO, respectively. The calculated $-dO_4/dZ$ are significantly larger than the mean
316 O4I fitting errors of 58, which implies that the O4I at 477 nm is useful in estimating
317 the AEH. The small fitting errors at 477 nm are due to the larger O₄ absorption and less
318 interferences by other trace gases in this spectral window.

319 Figure 5 shows $-dO_4/dZ$ as changing viewing geometries. As enlarging
320 geometrical path length for viewing geometry, $-dO_4/dZ$ also increases because the path
321 length through the aerosol layer is also increased. The mean value of $-dO_4/dZ$
322 including all cases of AEH is estimated to be 90 to 326 at SZA of 30.0 degree and VZA
323 of 30.0 degree, while it is estimated to be 265 to 485 at SZA of 60.0 degree and VZA
324 of 60.0 degree. Although aerosol scattering angle is changed by SZA and VZA, the
325 O4I sensitivity to AEH is generally increased to increasing optical path length to the
326 viewing geometries. From this result, the accuracy for the AEH retrieval is potentially
327 better for large zenith angle cases than for low zenith angle cases.

328

329 **3.2. Error analysis**

330 Errors are also estimated in terms of key variables in the estimation of the O4I at
 331 477 nm, with the variables and their dimensions as summarized in Table 3. For the
 332 error analysis of AEH retrieval, characteristics for all of extinction properties are
 333 essential to consider. In this study, errors are analyzed in terms of AOD, aerosol
 334 vertical distribution, particle size and SSA for aerosol amount and properties. Surface
 335 albedo variation is also considered to represent surface condition. To estimate the error
 336 amount, the AEH error is converted from the half of O4I difference between adding
 337 and deducting perturbation of variables as shown in equation (1).

$$338 \quad \varepsilon(Z) = \left| \frac{O4I(x+\delta x, Z) - O4I(x-\delta x, Z)}{2.0 \times dO4I/dZ(x, Z)} \right| \quad (1)$$

339 where $\varepsilon(Z)$ is the AEH error amount due to variable of error source, x , in AEH
 340 of Z , and δx is perturbation of AEH retrieval error source. The $\varepsilon(Z)$ value also
 341 depends on viewing geometries. Therefore $\varepsilon(Z)$ is represented for specific geometries
 342 together with averaging over all geometries.

343

344 **3.2.1. AOD**

345 The O4I at 477 nm has sensitivity not only for AEH but for AOD as shown in
 346 Figure 4(g) ~ (i). Because the radiance extinction by aerosol changes depending on
 347 AOD, the optical path length of TOA radiance is also affected by AOD. For different
 348 AODs (τ_a), the O4I at AEHs of 1.0 and 3.0 km is shown in Figure 6 for the same
 349 geometry assumed in Figure 4. From OMI standard products, the expected error of the
 350 AOD over ocean is the larger of 0.1 or 30% for absorbing aerosol, and the larger of 0.1
 351 or 20% for non-absorbing aerosol (Torres *et al.*, 1998, 2002). For this reason, the
 352 uncertainty of AOD is assumed to be 0.1 in this study, although uncertainty of AOD

353 would be larger than the assumed value for large AOD. The decreasing rate of the O4I
354 ($-dO_4/d\tau_a$), which defines O4I reduction with AOD increase by 0.1, is found to be
355 larger for the AEH at 3.0 km than for that at 1.0 km. Among the three aerosol types,
356 the $-dO_4/d\tau_a$ is found to be the least for the WASO, which has stronger scattering
357 characteristics than other two aerosol types. In addition, the sensitivity for WASO
358 showed negative $-dO_4/d\tau_a$ for small AOD at low AEH, which has small shielding
359 effect with large enhancement effect, due to the large SSA of WASO. The mean -
360 $dO_4/d\tau_a$ values are estimated to be 1.2%, 0.9%, and -0.1% for the AEH of 1.0 km as
361 the AOD changes by 0.1 for the MITR, COPO, and WASO, respectively, whereas they
362 are estimated to be 2.3%, 2.1%, and 1.0% for the AEH of 3.0 km with respect to the
363 same AOD changes for the three different type, respectively.

364 Figure 7 shows the expected error in AEH due to retrieval uncertainty of AOD
365 from observation. Because O_4 concentration exponentially decreases as the
366 atmospheric altitude increases, the sensitivity to AEH becomes weak at high AEHs. In
367 addition, aerosol signal is relatively weak for low AOD. From these reasons, the AEH
368 retrieval error due to AOD uncertainty is maximized for the high AEH with low AOD
369 cases for all aerosol types. The maximum retrieval error is 2.0, 0.7, and 4.4 km for
370 COPO, WASO, and MITR for the case at AEH of 4.0 km and AOD of 0.4, which is
371 least sensitive case for AEH. For AOD of 0.4, however, the retrieval error due to AOD
372 uncertainty is 0.3, 0.2, and 0.4 km for COPO, WASO, and MITR for the case at AEH
373 of 1.0 km. Except for AEH lower than 4 km and AOD larger than 0.4, the retrieval
374 error of AEH is less than 1.0 km for all viewing geometries and all aerosol types.

375 Furthermore, the AEH error for AOD uncertainty is also dependent on viewing
376 geometries. From previous studies, the error for cloud height information depends on

377 the observation geometries due to changing average optical path length (Accarreta *et*
378 *al.*, 2004; Chimot *et al.*, 2015). Moreover, the retrieval error sensitivity for observation
379 geometries is also found in aerosol height estimation by O₂-A band (Sanders *et al.*,
380 2015). Similar to these previous studies, the AEH error becomes larger for short light
381 paths and smaller for long paths. Figure 8 shows the viewing geometry dependence of
382 AEH error for AOD of 1.0. With the increase in effective optical path length, the
383 radiance signal from aerosol is also enhanced. In general, the AEH error decreases
384 with increasing viewing geometries. For WASO case, however, the AEH error is
385 smaller for short path length than long path length in low AEH case. For thin aerosol
386 layer situation, the radiance is enhanced by scattering aerosols which results in
387 increasing optical path length. In the small SZA and VZA, aerosol layer effectively
388 brings enhancement effect. With increasing SZA and VZA, however, the shielding
389 effect due to aerosol layer enhances because radiance has to pass through long path
390 through aerosol layer. For this reason, the smallest error case is inflection point of
391 AOD sensitivity, which corresponds to turnaround point between with larger shielding
392 effect than enhancement effect.

393

394 **3.2.2. SSA**

395 Torres *et al.* (1998) showed that the result of the SSA from OMI can be
396 overestimated due to the cloud contamination, although aerosol retrieval algorithm
397 considers the existence of cloud in sub-pixel. Furthermore, the SSA varies widely for
398 different aerosol types. Therefore, the sensitivity of O4I to the SSA variation is
399 estimated for the same geometries used in the previous tests. To estimate O4I
400 sensitivity to the SSA variation, the imaginary part of refractive index value

401 corresponding to 10% variability for SSA is changed after fixing the real part of
402 refractive index. The mean O4I changes by 106, 282, and 205 for MITR, WASO, and
403 COPO, respectively, with respect to its SSA deviation by 10%. To compare the
404 difference for WASO and COPO, it is proportional to the absolute values of the SSA
405 for all simulated cases. In addition, the difference for MITR is smaller than those for
406 COPO, because less fraction of back scattering in coarse mode particle makes less
407 sensitive to O4I.

408 Figure 9 shows the AEH error due to the SSA variation by 10%. Because of the
409 low sensitivity characteristics of AEH as shown in section 3.1, thus large errors are
410 shown for high AEH and low AOD cases. However, the AEH errors are less than 1 km
411 for COPO aerosol type. For AOD of 1.0, the AEH error due to SSA variation is
412 estimated to be 610 to 900 m for the COPO type. Furthermore, the error is calculated
413 to range from 270 to 1220 m and from 930 to 1400 m for COPO and WASO type,
414 respectively, if AEH is 3 km, frequently assumed reference altitude in aerosol retrieval
415 algorithm (e.g., Torres *et al.*, 1998). For MITR, dust-like type aerosol, AEH error,
416 which ranges from 410 to 1430 m for AOD of 1.0, is generally the largest compared to
417 those of other aerosol types. In general, uncertainty of aerosol optical properties is
418 large for thin aerosol layer case, thus that of the AEH is as well.

419

420 **3.2.3. Particle size**

421 Aerosol particle size has noticeable effects on the phase function, thus the
422 directional scattered intensity. However, most of aerosol retrieval algorithm assumes
423 aerosol particle size depending on its type as an input parameter to RTM calculation.
424 Although aerosol type is categorized, however, physical properties of aerosol can be

425 changed according to the source type and transport characteristics. In the OMI aerosol
426 algorithm, size distribution is one of error sources for the AOD (Torres *et al.*, 2002).

427 Figure 10 shows the AEH error due to particle size change. For error estimation,
428 mode radius difference for number size distribution is assumed to be $\pm 20\%$, which
429 corresponds to larger range by 4 times than those from the error budget study for OMI
430 standard product (Torres *et al.*, 2002). Overall, O4I difference is within the order of
431 100. The coarse mode aerosol, MITR in this study, results in the largest O4I difference
432 for all cases, thus the largest AEH error for MITR which is estimated to range from 0.2
433 to 2.7 km. On the other hand, the error ranges from 0.03 to 0.5 km and from 0.2 to 1.9
434 km for WASO and COPO, respectively. The largest AEH errors for the three aerosol
435 types are estimated for the case with AOD of 0.4 and AEH at 5.0 km.

436

437 **3.2.4. Surface Albedo**

438 As the surface albedo affects the $-dO_4/dZ$, the sensitivity of the O4I is also tested
439 with respect to the surface albedo difference of 0.02. The difference of climatological
440 surface albedo between that obtained from the total ozone monitoring spectrometer
441 (TOMS) and the global ozone monitoring experiment (GOME) was known to be up to
442 0.02 (Koelemeijer *et al.*, 2003). Table 4 shows the sensitivity of the O4I with respect to
443 the change in the surface albedo. The absolute difference of O4I due to surface albedo
444 variation is below 85. Because aerosol layer attenuates the reflected radiance from
445 surface, the absolute difference of O4I value decreases as aerosol amount increase.
446 Furthermore, it is found that the difference of O4I due to surface albedo change is
447 larger for the non-absorbing aerosol than the absorbing aerosol, because absorbing
448 aerosol attenuates the reflected radiance more than the non-absorbing aerosol. In terms

449 of AEH change, the O4I difference increases as AEH increase. For low AEH case,
450 optical path length of reflected radiance from surface to aerosol layer is relatively short
451 as compared to high AEH case. For this reason, the O4I sensitivity for surface albedo
452 is reduced by high concentration of aerosol near the surface for the low AEH case.

453 Figure 11 shows the expected retrieval error of AEH due to surface albedo
454 difference as changing AEH with respect to AOD and its types. As mentioned in
455 previous section, the $-dO_4/dZ$ is small in high AEH and low AOD cases. Furthermore,
456 the albedo sensitivity increases as AEH increases and AOD decreases. As a result, the
457 AEH error is frequently larger than 1 km for high AEH with small AOD, especially
458 when AOD is less than 0.4. Because reflected radiance from surface is dominant for
459 thin aerosol case, the AEH error in high AEH with low AOD shows the largest value as
460 compared to previous error analysis. However, the AEH error sharply decreases as
461 AOD increases and AEH decreases, when aerosol signal becomes dominant.
462 Especially for MITR, four simulation cases, when AOD = 0.4 with AEH > 3.0 km and
463 AOD = 1.0 with AEH = 5.0 km, show the AEH error larger than 1 km. Because -
464 dO_4/dZ is too small in these cases, AEH retrievals in the four simulation cases show
465 limitation as a reliable result. For COPO and WASO, however, all the cases in AEH <
466 3.0 km, which directly influence surface concentration, show error lower than 750 m
467 even for the assumed AOD of 0.4. In addition, errors less than 500 m are found for
468 AOD > 1.0 with AEH < 3.0 km.

469

470 **3.2.5. Vertical distribution**

471 Aerosol vertical distribution varies largely by distance from source, atmospheric
472 dynamics during aerosol transport, and sink mechanism in reality. To estimate the AEH

473 error due to variation of aerosol vertical distribution, the half-width of GDF
474 distribution was doubled for comparison. Although it is not possible here to consider
475 all kinds of aerosol vertical distributions due to its large variability in profile, aerosol
476 vertical distribution by changing the half-width of GDF distribution can reflect large-
477 scale changes in its vertical profile.

478 Table 5 shows the mean AEH errors between the two vertical profiles of aerosol
479 as AOD changes. As the aerosol vertical profile is changed with increasing its widths,
480 the difference of O4I ranges from 100 to 430. Because aerosol vertical profile
481 simultaneously affects aerosol concentration and layer thickness, the O4I difference
482 shows large value as the vertical distribution changes. For this reason, the AEH error is
483 larger than 2.5 km for all aerosol types with AOD of 0.4. The estimated errors caused
484 solely by the change between the two aerosol vertical profiles, range 1477 ± 602 ,
485 722 ± 190 , and 671 ± 265 m for the MITR, COPO, and WASO, respectively, for AOD
486 greater than 1.0.

487

488 **3.3. Error budget**

489 Table 6 shows the summary of the total error budget for the AEH estimation with
490 a list of the major error sources and their values, assuming errors in each variable in
491 OMI standard products. To convert the O4I difference to the AEH error, the difference
492 of O4I due to the respective error source is divided by that from the change of the AEH
493 in each bin of the AOD and AEH as shown in section 3.2, with the simulation cases
494 over 58,800 runs listed in Table 3 to calculate mean and standard deviation of errors.
495 Because of weak signal sensitivity to AEH for AOD of 0.4 and AEH at 5.0 km as
496 shown in the previous section, this simulation case is omitted in calculating statistical

497 values for error budget. In summary, the total number of aerosol simulations for the
498 combination of AOD and AEH includes 39 cases.

499 The mean errors from 10% variation in the SSA for all of the variable conditions
500 in Table 3 correspond to 726, 576, and 1047 m for the MITR, COPO, and WASO,
501 respectively. For the total error budget calculations, however, SSA change by 5% was
502 used according to Torres *et al.* (2007), which reported the variation of the SSA less
503 than 0.03 for the given aerosol type. The error from the vertical distribution is
504 estimated to be 720, 1480, and 690 m for the COPO, MITR and WASO, respectively.

505 The errors from SSA and aerosol profile shape are the two important error sources
506 in estimating the AEH, followed by the errors related to AOD and surface albedo.
507 From these results, the errors of the AEH due to the error from OMI AOD of 0.1 and
508 the surface albedo of 0.02 are less than 300 m for WASO and COPO, and about 400 m
509 for MITR. However, the AEH error from surface albedo is important for cases with
510 low AOD at high AEH, which is surface reflectance dominant case.

511 The mean errors from 20% variation in the aerosol particle size are 726, 576, and
512 1047 m for the MITR, COPO, and WASO, respectively. Torres *et al.* (2002) assumed
513 the variation of size distribution to be 5%. Thus, for the total error budget calculations
514 assuming 5% change in the particle size, the AEH errors are less than 100 m. In
515 addition, the errors in the O4I, and thereby the AEH, are associated with the variations
516 in the column amounts and the differences in the absorption cross section of each fitted
517 trace gas for the spectral analysis. The variations in the column amounts of trace gases
518 and the differences in the absorption cross section values do not affect significantly in
519 calculating the O4I. However, the O₄ vertical column density is changed by the change
520 in atmospheric pressure. In East Asia, the surface pressure over ocean is 1010.9 ± 29.6

521 (3-sigma) hPa from NCEP Reanalysis 2 data since 2004. In clear case, the difference
522 of O4I due to the $\pm 3\%$ for pressure variation is $3.4 \pm 0.1\%$ in all geometries.

523 Furthermore, the AEH error in terms of inaccurate spectral wavelength calibration
524 is estimated based on the assumed errors of ± 0.02 nm, which corresponds to 0.1 pixels
525 for OMI. Although it is well known that the accuracy in the spectral wavelength
526 calibration before the DOAS fitting affects the trace gas SCD retrieval, the errors in the
527 O4I associated with the wavelength shift of the sub-pixel scale are estimated to be
528 negligible due to the broad O₄ absorption band width around 477 nm.

529 Finally, the total error budget in the AEH retrieval is estimated based on the error
530 analysis with respect to error sources. Note that the result of error analysis explains
531 about 50% for SSA and 25% for size parameter in calculating the total error budget.
532 Overall, the total error budget in the AEH retrieval is estimated to be 739, 1276, and
533 846 m for the COPO, MITR, and WASO, respectively, with the exception of the
534 contribution of the errors in the aerosol vertical profiles. Therefore accurate
535 assumption for optical properties of aerosol is essential to develop the retrieval
536 algorithm of aerosol height.

537

538 **4. Case study**

539 To demonstrate the feasibility from real measurements, the AEHs are derived
540 using hyperspectral data from OMI. OMI channels are composed of UV-1 (270-314
541 nm), UV-2 (306-380 nm), and a visible wavelength range (365-500 nm) with a spectral
542 resolution (FWHM) of 0.63, 0.42, and 0.63 nm, respectively (Levelt *et al.*, 2006). The
543 spatial resolution is 13 km \times 24 km at nadir in "Global Mode". In the present study, the
544 OMI spectral data over the visible wavelength range are used to derive the O4I at 477

545 nm and the AEH information.

546 Figure 12 shows an AEH retrieval algorithm for the case study. In retrieving AEH,
547 AOD is obtained from MODIS standard product (e.g., Levy *et al.*, 2007). Although
548 OMI aerosol product provides AOD at 500 nm, AOD from OMI was partially affected
549 by aerosol height and suffered from cloud contamination due to its large footprint
550 (Torres *et al.*, 2002). For this reason, AOD from MODIS was allocated to the OMI
551 pixels as a reference AOD for the AEH retrieval. For type selection, the AE from
552 MODIS and AI from OMI is respectively used for the information of size and
553 absorptivity, to classify aerosol type into four following the method from Kim *et al.*
554 (2007) and Lee *et al.* (2007). After determining AOD and aerosol type, LUT, which is
555 generated as functions of geometries (SZA, VZA, and RAA), aerosol types and AODs,
556 is used to determine the AEH information by comparing simulated with the measured
557 O4I value. The variables and their dimensions for the LUT calculations are listed in
558 Table 7. Due to the limitation of the accuracy of aerosol type classification and those of
559 AOD over land, this study estimates the AEH only over ocean surface. Although
560 temporal and spatial variation of surface albedo influences the AEH result from error
561 study, surface albedo is assumed to be a fixed value of 0.10, which is used in the
562 sensitivity study. Even if the surface albedo is changed but known, the qualitative
563 conclusion here is not affected. For case study, the LUT of O4I is developed by the
564 aerosol model based on AERONET data over East Asia. Extensive AERONET dataset
565 over East Asia are used to provide represent aerosol optical properties for the LUT
566 calculation.

567 Figure 13 shows the results of the retrieved AEH during the Asian dust event on
568 March, 31, 2007. MODIS products of AOD and FMF on this date show that thick dust

569 layer with the AOD up to 1.0 from China to the Yellow Sea [Figure 13(b)] and the
570 FMF ranging from 0.2 to 0.4, indicating the dominance of coarse-mode particles
571 [Figure 13(c)]. Using the basis of the current algorithm with the pre-determined AOD
572 and type, the mean retrieved AEH is 2.3 ± 1.3 km over 647 pixels in East Asia [Figure
573 13(d)]. The retrieved result is compared with the backscattering intensity from the
574 CALIOP observation over the Yellow Sea as shown in Figure 13(e). From CALIOP
575 observation, the aerosol layer height over Yellow Sea is located at around 1 km altitude
576 for most of observed regions. Over the Yellow Sea domain in $35\sim 40^\circ\text{N}$ and $120\sim 130$
577 $^\circ\text{E}$, the AEH from OMI is 1.5 ± 1.1 km over 166 pixels, which is within 1 km difference
578 from the CALIOP. From the retrieved result, the retrieved AEH is successfully
579 retrieved within expected error, and the current algorithm quantitatively estimates the
580 AEH over East Asia.

581 Figure 14 is another case study of the retrieved AEH on February, 21, 2008.
582 MODIS products of AOD and FMF on this date show thick anthropogenic aerosol
583 transported with the AOD ranging from 0.6 to 1.0 [Figure 14(b)] and the FMF ranging
584 from 0.8 to 1.0 [Figure 14(c)] all over the Yellow Sea. The mean retrieved AEH is
585 1.4 ± 1.2 km over 1480 pixels in East Asia as shown in Figure 14(d). On this date,
586 CALIOP passed over coastal line between China and Yellow Sea. The aerosol layer
587 height ranged from 0.5 to 2.5 km during the overpass over East Asia as shown in
588 Figure 14(e). The AEH from OMI is 0.6 ± 0.4 km over 601 pixels in $30\sim 40^\circ\text{N}$ and
589 $120\sim 125^\circ\text{E}$. Contrary to large spatial variation of the AEH from CALIOP, the AEH
590 from OMI shows spatially stable values on this date.

591 Figure 15 shows the scatter plot of AEH between CALIOP and OMI on the dates
592 in Table 8, which lists aerosol transport cases over East Asia with simultaneous

593 observations by OMI and CALIOP in 2007 and 2008. The AEH from CALIOP is
594 estimated by the data from vertical profile of aerosol extinction coefficient at 532 nm.
595 Because the O4I sensitivity for AEH is not large at AEH higher than 4 km, the
596 comparison test was limited to cases with AEH less than 4.5 km from OMI. For data
597 collocation, the latitude and longitude difference between two sensors are within 0.25
598 degree. Figure 15(a) shows the comparison of AEH from OMI and CALIOP with
599 MODIS AOD larger than 0.5. It is assumed that the reference expected error (EE) is 1
600 km (Fishman *et al.*, 2012). Almost 60% of retrieved pixel shows the AEH result within
601 the EE. Because of large AEH error for low AOD, the accuracy of AEH result from
602 OMI is poor. Furthermore, this case study assumes constant surface albedo value over
603 ocean. However, ocean surface albedo is also changed by turbidity due to sediments
604 and ocean surface due to wind. For this reason, the AEH error is exaggerated for low
605 AOD cases. If lower of AOD for the comparison is set to be 1.0, the proportion of
606 pixel within EE improves up to 80% as shown in Figure 15(b). Furthermore, the
607 correlation of the AEH between the two sensors is improved with the regression line
608 slope of 0.62 and the correlation coefficient (R) of 0.65 for thick aerosol layer cases.
609 Therefore, the AEH algorithm from OMI provides the reasonable information about
610 the parameter of aerosol vertical distribution, if accurate aerosol model is provided for
611 the forward calculation.

612

613 **5. Summary & discussion**

614 The sensitivities of the O4I at 340, 360, 380, and 477 nm bands are investigated
615 with RTM calculations to derive the AEH using the space-borne hyperspectral data.
616 Among these O₄ absorption bands, the O4I at 477 nm is considered to be suitable for

617 the AEH retrieval. In addition to the AEH, AOD, aerosol type, aerosol vertical profile,
618 particle size, and surface albedo are also found to have effects on the O4I at 477 nm,
619 while the spectral calibration and cross section of the atmospheric gases have
620 negligible effects on the O4I. The major error source for the AEH retrieval is found to
621 be the uncertainty in SSA, which leads to the AEH error ranging from 270 to 1400 m
622 with the SSA perturbation by 10%. In addition, the profile shape is also a major error
623 source for the AEH estimation. According to the error estimations, the total errors are
624 739, 1276 m, and 846 m for absorbing, dust, and non-absorbing aerosol, respectively,
625 due to combined uncertainties of the variation from AOD, SSA, particle size, and
626 surface albedo.

627 In addition to the sensitivity analysis, an algorithm for the AEH derivation is
628 developed for the first time based on a LUT that consists of the O4I in terms of the
629 AEH, AOD, aerosol types, surface albedo, and measurement geometries. After the
630 determination of AOD and aerosol types from the MODIS, the AEH value is derived
631 over East Asia by the current algorithm using OMI measurement data. Considering the
632 accuracy of AOD and aerosol types, the result is shown over ocean surface. From
633 several cases for the long-range transport of aerosol over East Asia, the derived AEH
634 shows reasonable value as compared to aerosol layer height from CALIOP with the
635 correlation coefficient of 0.62 for AOD larger than 1.0. In addition, 80% of estimated
636 AEH from OMI showed error less than 1 km in AEH.

637 There are many works to be done to improve the newly introduced algorithm as it
638 requires the products from MODIS to determine the AOD and aerosol types prior to
639 the AEH retrieval. The vertical distribution and the optical properties of the aerosol
640 need to be quantified using the combination of observation database, such as MPLNET

641 and AERONET. Furthermore, the spatial variation of the AOD, surface pressure and
642 the contamination by the cloud in the sub-pixel scale need to be investigated as they
643 are also thought to affect the retrieved results. If the surface reflectance can be
644 characterized with sufficient accuracy, the retrieval of the AEH can be extended to over
645 land. In addition, the O4I method in this study can be applied to the surface pressure
646 estimation in clear regions.
647

648 **Acknowledgements**

649 This work was supported by the Eco Innovation Program of KEITI
650 (ARQ201204015), Korea, and it was also supported by the Brain Korea plus program.

651

652 **References**

653 Accarreta, J. R., de Haan, J. F., and Stammes, P.: Cloud pressure retrieval using the O₂-
654 O₂ absorption band at 477 nm, *J. Geophys. Res.*, *109*, D05204,
655 doi:10.1029/2003JD003915, 2004

656 Ahn, C., Torres, O., and Jethva, H.: Assessment of OMI near-UV aerosol optical depth
657 over land, *J. Geophys. Res.*, *119*, 2457-2473, doi:10.1002/2013JD020188, 2014.

658 Albrecht, B. A.: Aerosols, cloud microphysics, and fractional cloudiness, *Science*, *245*,
659 1227-1230, 1989.

660 Bogumil, K., Orphal, J., Burrows, J. P., and Flaud, J. M.: Vibrational progressions in the
661 visible and near-ultraviolet absorption spectrum of ozone, *Chem. Phys. Lett.*,
662 *349*, 241-248, 2001.

663 Castellanos, P., Boersma, K. F., Torres, O., and de Haan, J. F.: OMI tropospheric NO₂
664 air mass factors over South America: effects of biomass burning aerosols, *Atmos.*
665 *Meas. Tech. Discuss*, *8*, 2683-2733, 2015.

666 Chiang, C. -W, Chen, W. -N., Liang, W. -A., Das, S. K., and Nee, J.-B.: Optical
667 properties of tropospheric aerosols based on measurements of lidar, sun-
668 photometer and visibility at Chung-Li (25°N, 121°E), *Atmos. Env.*, *41*, 4128-
669 4137, 2007.

670 Chimot, J., Vlemmix, T., Veefkind, J. P., de Haan, J. F., and Levelt, P. F.: Impact of
671 aerosols on the OMI tropospheric NO₂ retrievals over industrialized regions:
672 how accurate is the aerosol correction of cloud-free scenes via a simple cloud
673 model?, *Atmos. Meas. Tech. Discuss*, *8*, 8385-8437, 2015.

674 Chou, M. -D, Chan, P. -K., and Wang, M.: Aerosol radiative forcing derived from
675 SeaWiFS-Retrieved aerosol optical properties, *J. Atmos. Sci.*, *59*, 748-757, 2002.

676 Christopher, S. A., Zhang, J., Kaufman, Y. J., and Remer, L. A.: Satellite-based
677 assessment of top of atmosphere anthropogenic aerosol radiative forcing over

678 cloud-free oceans, *Geophys. Res. Lett.*, 33, L15816, doi:10.1029/2005GL025535,
679 2006.

680 Chu, D. A.: Analysis of the relationship between MODIS aerosol optical depth and
681 PM2.5 in the summertime US., *Optics & Photonics. International Society for*
682 *Optics and Photonics*, 2006.

683 Chung, E. C., Ramanathan, V., Kim, D., and Podgorny. I. A.: Global anthropogenic
684 aerosol direct forcing derived from satellite and ground-based observations, *J.*
685 *Geophys. Res.*, 110, D24207, doi:10.1029/2005JD006356, 2005.

686 Clemer, K., van Roozendaal, M., Fayt, C., Hendrick, F., Hermans, C., Pinardi, G., Spurr,
687 R., Wang, P., and De Maziere, M.: Multiple wavelength retrieval of tropospheric
688 aerosol optical properties from MAXDOAS measurements in Beijing, *Atmos. Meas.*
689 *Tech.*, 3, 863-878, doi:10.5194/amt-3-863-2010, 2010.

690 Curier, R. L., Veeffkind, J. P., Braak, R., Veihelmann, B., Torres, O., and de Leeuw, G.:
691 Retrieval of aerosol optical properties from OMI radiances using a
692 multiwavelength algorithm: Application to western Europe, *J. Geophys. Res.*, 113,
693 D17S90, doi:10.1029/2007JD008738, 2008.

694 Dirksen, R. J., Boersma, K. F., de Laat, J., Stammes, P., van der Werf, G. R., Martin, M.
695 V., and Kelder, H. M., An aerosol boomerang: Rapid around-the-world transport of
696 smoke from the December 2006 Australian forest fires observed from space, *J.*
697 *Geophys. Res.*, 114, D21201, doi:10.1029/2009JD012360, 2009.

698 Dubovik, O., Holben, B., Eck, T. F., Smirnov, A., Kaufman, Y. J., King, M. D., Tanre, D.,
699 and Slutsker, I.: Variability of absorption and optical properties of key aerosol
700 types observed in worldwide locations, *J. Atmos. Sci.*, 59, 590-608, 2002.

701 Dubuisson, P., Frouin, R., Dessaily, D., Duforet, L., Leon, J. -F., Voss, K., and Antoine,
702 D.: Estimating the altitude of aerosol plumes over the ocean from reflectance ratio
703 measurements in the O2 A-band, *Remote Sens. Environ.*, 113, 1899-1911,
704 doi:10.1016/j.rse.2009.04.018, 2009.

705 Fish, D. J., and Jones, R. L.: Rotational Raman scattering and the ring effect in zenith-
706 sky spectra, *Geophys. Res. Lett.*, 22, 811-814, 1995.

707 Fishman, J., Iraci, L. T., Al-Saadi, J., Chance, K., Chavez, F., Chin, M., Coble, P., Davis,
708 C., DiGiacomo, P. M., Edwards, D., Eldering, A., Goes, J., Herman, J., Hu, C.,
709 Jacob, D. J., Jordan, C., Kawa, S. R., Key, R., Liu, X., Lohrenz, S., Mannino, A.,

710 Natraj, V., Neil, D., Neu, J., Newchurch, M., Pickering, K., Salisbury, J., Sosik, H.,
711 Subramaniam, A., Tzortziou, M., Wang, J., and Wang, M.: The United States' Next
712 Generation of Atmospheric Composition and Coastal Ecosystem Measurements:
713 NASA's Geostationary Coastal and Air Pollution Events (GEO-CAPE) Mission.
714 *Bull. Amer. Meteor. Soc.*, *93*, 1547-1566, 2012.

715 Friess, U., Monk, P. S., Remedios, J. J., Rozanov, A., Sinreich, R., Wagner, T., and Platt,
716 U.: MAX-DOAS O₄ measurements: A new technique to derive information on
717 atmospheric aerosols: 2. Modeling studies, *J. Geophys. Res.*, *111*, D14203,
718 doi:10.1029/2005JD006618, 2006.

719 Hayasaka, T., Satake, S., Shimizu, A., Sugimoto, N., Matsui, I., Aoki, K., and Muraji, Y.:
720 Vertical distribution and optical properties of aerosols observed over Japan during
721 the Atmospheric Brown Clouds-East Asia Regional Experiment 2005, *J. Geophys.*
722 *Res.*, *112*, D22S35, doi:10.1029/2006JD008086, 2007.

723 Haywood, J. M. and Shine, K. P.: The effect of anthropogenic sulfate and soot aerosol
724 on the clear sky planetary radiation budget, *Geophys. Res. Lett.*, *22*, 603-606, 1995.

725 Herman, J. R., Bhartia, P. K., Torres, O., Hsu, C., Seftor, C., and Celarier, E.: Global
726 distribution of UV-absorbing aerosols from Nimbus-7/TOMS data, *J. Geophys.*
727 *Res.*, *102*(D14), 16911-16922, 1997.

728 Hermans, C., Vandaele, A. C., Carleer, M., Fally, S., Colin, R., Jenouvrier, A., Coquart,
729 B., and Merienne, M.: Absorption Cross-sections of atmospheric constituents: NO₂,
730 O₂, and H₂O, *Environ. Sci. Poll. Res.*, *6*(3), 151-158, 1999.

731 Hermans, C., Vandaele, A. C., Fally, S., Carleer, M., Colin, R., Coquart, B., Jenouvrier,
732 A., and Merienne, M. F.: Absorption cross-section of the collision-induced bands
733 of oxygen from the UV to the NIR. In Weakly interacting molecular pairs:
734 unconventional absorbers of radiation in the atmosphere, (pp. 193-202), Springer
735 Netherlands, 2003.

736 Hess, M., Koepke, P., and Schult, I.: Optical properties of aerosols and clouds: The
737 software package OPAC, *B. Am. Meteorol. Soc.*, *79*(5), 831-844, 1998.

738 Higurashi, A., and Nakajima, T.: Detection of aerosol types over the East China Sea
739 near Japan from four-channel satellite data, *Geophys. Res. Lett.*, *29*(17), 1836,
740 doi:10.1029/2002GL015357, 2002.

741 Holzer-Popp, T., and Schroedter-Homscheidt, M.: Synergetic aerosol retrieval from
742 ENVISAT. In Proc. ERS/ENVISAT Symposium, Salzburg (Vol. 6, No. 10.9), 2004.

743 Hutchison, K. D., Smith, S., and Faruqi, S. J.: Correlating MODIS aerosol optical
744 thickness data with ground-based PM_{2.5} observations across Texas for use in a
745 real-time air quality prediction system, *Atmos. Env.*, *39*, 7190-7203, 2005.

746 Irie, H., Kanaya, Y., Akimoto, H., Iwabuchi, H., Shimizu, A., and Aoki, K.: Dual-
747 wavelength aerosol vertical profile measurements by MAX-DOAS at Tsukuba,
748 Japan, *Atmos. Chem. Phys.*, *9*, 2741-2749, 2009.

749 Irie, H., Takashima, H., Kanaya, Y., Boersma, K. F., Gast, L., Wittrock, F., Brunner, D.,
750 Zhou, Y., and van Roozendaal, M.: Eight-component retrievals from ground-based
751 MAX-DOAS observations, *Atmos. Meas. Tech.*, *4*, 1027-1044, 2011.

752 Irie, H., Nakayama, T., Shimizu, A., Yamazaki, A., Nagai, T., Uchiyama, A., Zaizen, Y.,
753 Kagamitani, S., and Matsumi, Y.: Evaluation of MAX-DOAS aerosol retrievals by
754 coincident observations using CRDS, lidar, and sky radiometer in Tsukuba, Japan,
755 *Atmos. Meas. Tech.*, *8*, 2775-2788, 2015.

756 Jeong, M., -J., and Hsu, N. C.: Retrievals of aerosol single-scattering albedo and
757 effective aerosol layer height for biomass-burning smoke: Synergy derived from
758 “A-Train” sensors, *Geophys. Res. Lett.*, Vol. 35, L24801,
759 doi:10.1029/2008GL036279, 2008.

760 Jethva, H., Torres, O., and Ahn, C.: Global assessment of OMI aerosol single-scattering
761 albedo using ground-based AERONET inversion, *J. Geophys. Res.*, *119*, 9020-
762 9040, doi:10.1002/2014JD021672, 2014.

763 Johnson, B. T., Heese, B., McFarlane, S. A., Chazette, P., Jones, A., and Bellouin, N.:
764 Vertical distribution and radiative effects of mineral dust and biomass burning
765 aerosol over West Africa during DABEX, *J. Geophys. Res.*, *113*, D00C12,
766 doi:10.1029/2008JD009848, 2008.

767 Jones, A., Roberts, D. L., and Slingo, A.: A climate model study of indirect radiative
768 forcing by anthropogenic sulphate aerosols, *Nature*, *370*, 450-453, 1994.

769 Jones, T. A., and Christopher, S. A.: MODIS derived fine mode fraction characteristics
770 of marine, dust, and anthropogenic aerosols over the ocean, constrained by
771 GOCART, MOPITT, and TOMS, *J. Geophys. Res.*, *112*, D22204,
772 doi:10.1029/2007JD008974, 2007.

773 Kaufman, Y. J., Tanre, D., and Boucher, O.: A satellite view of aerosols in the climate
774 system, *Nature*, 419, 215-223, 2002.

775 Kim, J., Lee, J., Lee, H. C., Higurashi, A., Takemura, T., and Song, C. H.: Consistency
776 of the aerosol type classification from satellite remote sensing during the
777 Atmospheric Brown Cloud – East Asia Regional Experiment campaign, *J.*
778 *Geophys. Res.*, 112, D22S33, doi:10.1029/2006JD008201, 2007.

779 Kleipool, Q. L., Dobber, M. R., de Haan, J. F., and Levelt, P. F.: Earth surface
780 reflectance climatology from 3 years of OMI data, *J. Geophys. Res.*, 113,
781 D18308, doi:10.1029/2008JD010290, 2008.

782 Koelemeijer, R. B. A., de Haan, J. F., and Stammes, P.: A database of spectral surface
783 reflectivity in the range 335-772 nm derived from 5.5 years of GOME
784 observations, *J. Geophys. Res.*, 108(D2), 4070, doi:10.1029/2002JD002429,
785 2003.

786 Kokhanovsky, A. A., and Rozanov, V. V.: The determination of dust cloud altitudes from
787 a satellite using hyperspectral measurements in the gaseous absorption band, *Int. J.*
788 *Rem. Sens.*, 31, Nos. 9-10, 2729-2744, 2010.

789 Koppers, G. A. A., and Murtagh, D. P.: Retrieval of height resolved aerosol optical
790 thickness in the atmospheric band (Chapter 5), in G. A. A. Koppers, Radiative
791 transfer in the absorption bands of oxygen: Studies of their significance in ozone
792 chemistry and potential for aerosol remote sensing, Stockholm Univ., Stockholm,
793 Sweden, 1997.

794 Labonne, M., Breon, F. -M., and Chevallier, F.: Injection height of biomass burning
795 aerosols as seen from a spaceborne lidar, *Geophys. Res. Lett.*, 34, L11806,
796 doi:10.1029/2007GL029311, 2007.

797 Lee, H., Irie, H., Kim, Y. J., Noh, Y., Lee, C., Kim, Y., and Chun, K. J.: Retrieval of
798 aerosol extinction in the lower troposphere based on UV MAX-DOAS
799 measurements, *Aerosol Sci. Technol.*, 43(5), 502-509, 2009.

800 Lee, H., Irie, H., Gu, M., Kim, J., and Hwang, J.: Remote sensing of tropospheric
801 aerosol using UV MAX-DOAS during hazy conditions in winter: Utilization of O4
802 absorption bands at wavelength intervals of 338-368 and 367-393 nm, *Atmos. Env.*,
803 doi:10.1016/j.atmosenv.2011.07.019, 2011.

804 Lee, J., Kim, J., Lee, H. C., and Takemura, T.: Classification of aerosol type from
805 MODIS and OMI over East Asia, *Asia-Pacific J. Atmos. Sci.*, *43*, 4, 343-357, 2007.

806 Lee, J., Kim, J., Song, C. H., Ryu, J. -H., Ahn, Y. -H., and Song, C. K.: Algorithm for
807 retrieval of aerosol optical properties over the ocean from the Geostationary Ocean
808 Color Imager, *Remote Sens. Environ.*, *114*, 1077-1088, 2010.

809 Levelt, P. F., van den Oord, G. H. J., Dobber, M. R., Maelkki, A., Visser, H., de Vries, J.,
810 Stammes, P., Lundell, J. O. V., and Saari, H.: The Ozone Monitoring Instrument,
811 *IEEE T. Geosci. Remote.*, *44*(5), 1093-1101, 2006.

812 Levy, R. C., Remer, L. A., Mattoo, S., Vermote, E. F., and Kaufman, Y. J.: Second-
813 generation operational algorithm : Retrieval of aerosol properties over land from
814 inversion of Moderate Resolution Imaging Spectroradiometer spectral
815 reflectance, *J. Geophys. Res.*, *112*, D13211, doi:10.1029/2006JD007811, 2007.

816 Li, X., Brauers, T., Shao, M., Garland, R. M., Wagner, T., Deutschmann, T., and Wahner,
817 A.: MAX-DOAS measurements in southern China: Retrieval of aerosol
818 extinctions and validation using ground-based in-situ data, *Atmos. Chem. Phys.*,
819 *10*, 2079-2089, 2010.

820 Lin, J. -T., Martin, R. V., Boersma, K. F., Sneep, M., Stammes, P., Spurr, R., Wang, P.,
821 van Roozendaal, M., Clemer, K., and Irie, H.: Retrieving tropospheric nitrogen
822 dioxide from the Ozone Monitoring Instrument: effects of aerosols, surface
823 reflectance anisotropy, and vertical profile of nitrogen dioxide, *Atmos. Chem.*
824 *Phys.*, *14*, 1441-1461, 2014.

825 Lin, J. -T., Liu, M. -Y., Xin, J. -Y., Boersma, K. F., Spurr, R., Martin, R., and Zhang, Q.:
826 Influence of aerosols and surface reflectance on satellite NO₂ retrieval: seasonal
827 and spatial characteristics and implications for NO_x emission constraints, *Atmos.*
828 *Chem. Phys. Discuss.*, *15*, 12653-12714, 2015.

829 Liu, Y., Sarnat, J. A., Kilaru, V., Jacob, D. J., and Koutrakis, P.: Estimating ground-level
830 PM_{2.5} in the Eastern United States using satellite remote sensing, *Environ. Sci.*
831 *Technol.*, *39*, 3269-3278, 2005.

832 Nakajima, T., and Higurashi, A.: A use of two-channel radiances for and aerosol
833 characterization from space, *Geophys. Res. Lett.*, *25*(20), 3815-3818, 1998.

834 Newnham, D. A., and Ballard, J.: Visible absorption cross sections and integrated
835 absorption intensities of molecular oxygen (O₂ and O₄), *J. Geophys. Res.*, *103*, No.
836 D22, 28801-28816, 1998.

837 Omar, A. H., Winker, D. M., Kittaka, C., Vaughan, M. A., Liu, Z., Hu, Y., Treppe, C. R.,
838 Rogers, R. R., Ferrare, R. A., Lee, K. -P., Kuehn, R. E., and Hostetler, C. A.: The
839 CALIPSO automated aerosol classification and lidar ratio selection algorithm, *J.*
840 *Atmos. Oceanic Technol.*, Vol. 26, 1994-2014, 2009.

841 Payne, R. E.: Albedo of the Sea Surface, *J. Atmos. Sci.*, *29*, 959-970, 1972.

842 Platt, U.: Differential optical absorption spectroscopy (DOAS), *Air monitoring by*
843 *spectroscopic technique*, *127*, 27-84, 1994.

844 Platt, U., and Stutz, J.: *Differential absorption spectroscopy*, Springer Berlin Heidelberg,
845 2008.

846 Prospero, J. M.: Long-term measurements of the transport of African mineral dust to the
847 southeastern United States: Implications for regional air quality, *J. Geophys.*
848 *Res.*, *104(D13)*, 15917-15927, 1999.

849 Reid, J. S., Westphal, D. L., Livingston, J. M., Savoie, D. L., Maring, H. B., Jonsson, H.
850 H., Eleuterio, D. P., Kinney, J. E., Reid, E. A.: Dust vertical distribution in the
851 Caribbean during the Puerto Rico Dust Experiment, *Geophys. Res. Lett.*, *29*, 7,
852 1151, doi:10.1029/2001GL014092, 2002.

853 Remer, L. A., Kleidman, R. G., Levy, R. C., Kaufman, Y. J., Tanre, D., Mattoo, S.,
854 Martins, J. V., Ichoku, C., Koren, I., Yu, H., and Holben, B. N.: Global aerosol
855 climatology from the MODIS satellite sensors, *J. Geophys. Res.*, *113*, D14S07,
856 doi:10.1029/2007JD009661, 2008.

857 Sanders, A. F. J. and de Haan, J. F.: Retrieval of aerosol parameters from the oxygen A
858 band in the presence of chlorophyll fluorescence, *Atmos. Meas. Tech.*, *6*, 2725-
859 2740, 2013.

860 Sanders, A. F. J., de Haan, J. F., Sneep, M., Apituley, A., Stammes, P., Vieitez, M. O.,
861 Tilstra, L. G., Tuinder, O. N. E., Koning, C. E., and Veefkind, J. P.: Evaluation of
862 the operational Aerosol Layer Height retrieval algorithm for Sentinel-5
863 Precursor: application to O₂ A band observations from GOME-2A, *Atmos. Meas.*
864 *Tech.*, *8*, 4947-4977, 2015.

865 Sanghavi, S., Martonchik, J. V., Landgraf, J., and Platt, U.: Retrieval of optical depth
866 and vertical distribution of particulate scatterers in the atmosphere using O2 A-
867 and B-band SCIAMACHY observations over Kanpur: a case study, *Atmos. Meas.*
868 *Tech.*, 5, 1099-1119, 2012.

869 Sasano, Y.: Tropospheric aerosol extinction coefficient profiles derived from scanning
870 lidar measurements over Tsukuba, Japan, from 1990 to 1993, *App. Opt.*, 35(24),
871 4941-4952, 1996.

872 Seo, S., Kim, J., Lee, H., Jeong, U., Kim, W., Holben, B. N., Kim, S., Song, C. H., and
873 Lim, J. H.: Estimation of PM₁₀ concentrations over Seoul using multiple
874 empirical models with AERONET and MODIS data collected during the
875 DRAGON-Asia campaign, *Atmos. Chem. Phys.*, 15, 1-16, doi:10.5194/acp-15-
876 1-2015, 2015.

877 Shimizu, A., Sugimoto, N., Matsui, I., Arao, K., Uno, I., Murayama, T., Kagawa, N.,
878 Aoki, K., Uchiyama, A., and Yamazaki, A.: Continuous observation of Asian
879 dust and other aerosols by polarization lidars in China and Japan during ACE-
880 Asia, *J. Geophys. Res.*, 109, D19S17, doi:10.1029/2002JD003253, 2004.

881 Sneep, M., de Haan, J. F., Stammes, P., Wang, P., Vanbauce, C., Joiner, J., Vasilkov, A.
882 P., and Levelt, P. F.: Three-way comparison between OMI and PARASOL cloud
883 pressure products, *J. Geophys. Res.*, 113, D15S23, doi:10.1029/2007JD008694,
884 2008.

885 Spurr, R. J. D., Kurosu, T. P., and Chance, K. V.: A linearized discrete ordinate radiative
886 transfer model for atmospheric remote-sensing retrieval, *J. Quant. Spectro. Rad.*
887 *Trans.*, 68, 689-735, 2001.

888 Spurr, R. J. D.: Simultaneous derivation of intensities and weighting functions in a
889 general pseudo-spherical discrete ordinate radiative transfer treatment, *J. Quant.*
890 *Spectro. Rad. Trans.*, 75, 129-175, 2002.

891 Spurr, R. J. D.: VLIDORT: A linearized pseudo-spherical vector discrete ordinate
892 radiative transfer code for forward model and retrieval studies in multilayer
893 multiple scattering media, *J. Quant. Spectro. Rad. Trans.*, 102, 316-342, 2006.

894 Spurr, R., and Christi, M.: On the generation of atmospheric property Jacobians from
895 the (V)LIDORT linearized radiative transfer models, *J. Quant. Spectro. Rad. Trans.*,
896 142, 109-115, 2014.

897 Stutz, J., and Platt, U.: Numerical analysis and estimation of the statistical error of
898 differential optical absorption spectroscopy measurements with least-squares
899 methods, *Applied Optics*, 35, 30, 6041-6053, 1996.

900 Torres, O., Bhartia, P. K., Herman, J. R., Ahmad, Z., and Gleason, J.: Derivation of
901 aerosol properties from satellite measurements of backscattered ultraviolet
902 radiation: Theoretical basis, *J. Geophys. Res.*, 103(14), 17099-17110, 1998.

903 Torres, O., Decae, R., Veefkind, P., and de Leeuw, G.: *OMI Aerosol Retrieval Algorithm*,
904 OMI Algorithm Theoretical Basis Document, Vol. III, Clouds, Aerosols and
905 Surface UV Irradiance, NASA-KNMI ATBD-OMI-03, pp. 47-71, 2002.

906 Torres, O., Bhartia, P. K., Sinyuk, A., Welton, E. J., and Holben, B. N.: Total Ozone
907 Mapping Spectrometer measurements of aerosol absorption from space:
908 Comparison to SAFARI 2000 ground-based observations, *J. Geophys. Res.*, 110,
909 D10S18, doi:10.1029/2004JD004611, 2005.

910 Torres, O., Tanskanen, A., Veihelmann, B., Ahn, C., Braak, R., Bhartia, P. K., Veefkind,
911 P., and Levelt, P.: Aerosols and surface UV products from Ozone Monitoring
912 Instrument observations: An overview, *J. Geophys. Res.*, 112, D24S47,
913 doi:10.1029/2007JD008809, 2007.

914 Twomey, S. A., Piepgrass, M., and Wolfe, T. L.: An assessment of the impact of
915 pollution on the global albedo, *Tellus*, 36B, 356-366, 1984.

916 United States Committee on Extension to the Standard Atmosphere: *US Standard*
917 *Atmosphere 1976*, National Oceanic and Atmospheric Administration, NASA.,
918 United States Air Force, Washington DC, USA, 1976.

919 van Roozendaal, M., and Fayt, C.: *WinDOAS 2.1 Software user manual*, Uccle,
920 IASB/BIRA, 2001.

921 Vandaele, A. C., Hermans, C., Simon, P. C., Carleer, M., Colin, R., Fally, S., Merienne,
922 M. F., Jenouvrier, A., and Coquart, B.: Measurements of the NO₂ absorption cross-
923 section from 42000 cm⁻¹ to 10000 cm⁻¹ (238-1000 nm) at 220 K and 294 K, *J.*
924 *Quant. Spectrosc. Radiat. Transfer*, 59, 3-5, 171-184, 1998.

925 Veefkind, J. P., de Leeuw, G., Durkee, P. A., Russell, P. B., Hobbs, P. V., and Livingston,
926 J. M.: Aerosol optical depth retrieval using ATSR-2 and AVHRR data during
927 TARFOX, *J. Geophys. Res.*, 104(D2), 2253-2260, 1999.

928 Veihelmann, B., Levelt, P. F., Stammes, P., and Veefkind, J. P.: Simulation study of the
929 aerosol information content in OMI spectral reflectance measurements, *Atmos.*
930 *Chem. Phys.*, *7*, 3115-3127, 2007.

931 Wagner, T., Dix, B., Friedeburg, C. V., Friess, U., Sanghavi, S., Sinreich, R., and Platt,
932 U.: MAX-DOAS O₄ measurements: A new technique to derive information on
933 atmospheric aerosols- Principles and information content, *J. Geophys. Res.*, *109*,
934 D22205, doi:10.1029/2004JD004904, 2004.

935 Wagner, T., Beirle, S., Deutschmann, T., Grzegorski, M., and Platt, U.: Satellite
936 monitoring of different vegetation types by differential optical absorption
937 spectroscopy (DOAS) in the red spectral range, *Atmos. Chem. Phys.*, *7*, 69-79,
938 2007.

939 Wagner, T., Deutschmann, T., and Platt, U.: Determination of aerosol properties from
940 MAX-DOAS observations of the Ring effect, *Atmos. Meas. Tech.*, *2*, 495-512,
941 2009.

942 Wagner, T., Beirle, S., Deutschmann, T., and de Vries, M. P.: A sensitivity analysis of
943 Ring effect to aerosol properties and comparison to satellite observations, *Atmos.*
944 *Meas. Tech.*, *3*, 1723-1751, 2010.

945 Wang, J., and Christopher, S. A.: Intercomparison between satellite-derived aerosol
946 optical thickness and PM_{2.5} mass: Implications for air quality studies, *Geophys.*
947 *Res. Lett.*, *30*(21), 2095, doi:10.1029/2003GL018174, 2003.

948 Wang, P., Tuinder, O. N. E., Tilstra, L. G., and Stammes, P.: Interpretation of FRESCO
949 cloud retrievals in case of absorbing aerosol events, *Atmos. Chem. Phys.*, *12*,
950 9057-9077, 2012.

951 Watson, J. G., Chow, J. C., Lu, Z., Fujita, E. M., Lowenthal, D. H., Lawson, D. R., and
952 Ashbaugh, L. L.: Chemical mass balance source apportionment of PM₁₀ during
953 the Southern California air quality study, *Aerosol Sci. Technol.*, *21*(1), 1-36,
954 1994.

955 Yang, K., Liu, X., Bhartia, P. K., Krotkov, N. A., Carn, S. A., Hughes, E. J., Krueger, A.
956 J., Spurr, R. J. D., and Trahan, S. G.: Direct retrieval of sulfur dioxide amount
957 and altitude from spaceborne hyperspectral UV measurements: Theory and
958 application, *J. Geophys. Res.*, *115*, D00L09, doi:10.1029/2010JD013982, 2010.

959 Zhang, H., Lyapustin, A., Wang, Y., Kondragunta, S., Laszlo, L., Ciren, P., and Hoff, R.
960 M.: A multi-angle aerosol optical depth retrieval algorithm for geostationary
961 satellite data over the United States, *Atmos. Chem. Phys.*, *11*, 11977-11991, 2011.
962

963 **List of Tables**

964 Table 1. The database of cross section used for DOAS fitting analysis.

965 Table 2. Dimensions of LUT for the clear sky comparison.

966 Table 3. Dimensions of simulation cases for the error analysis of the AEH retrieval.

967 Table 4. Absolute difference of O4I for changing surface albedo by 0.02.

968 Table 5. The error for AEH due to the change in aerosol vertical distribution.

969 Table 6. Summary of error sources and total error budget for the AEH retrieval.

970 Table 7. Dimensions of LUT for the AEH algorithm using OMI.

971 Table 8. List of aerosol transport cases and its period for comparison.

972

973 **List of Figures**

- 974 Figure 1. Flowchart of the simulated O₄ SCD estimation.
- 975 Figure 2. Comparison of O₄ SCD directly retrieved from OMI radiance with the OMI
976 standard product on March 31, 2007.
- 977 Figure 3. Comparison of the O₄ SCD at 477 nm between the OMI standard product and
978 the calculated value from LUT (a) before and (b) after correction of LER.
- 979 Figure 4. The O4I at 360 nm band for (a) MITR, (b) WASO, and (c) COPO, (d) at 380
980 nm band for MITR, (e) WASO, and (f) COPO, and (g) at 477 nm band for MITR, (h)
981 WASO, and (i) COPO as a function of AEH.
- 982 Figure 5. The AEH sensitivity to O4I ($-dO_4/dZ$) with changing observation geometries
983 at 477 nm.
- 984 Figure 6. The O4I of (a) MITR, (b) WASO, and (c) COPO types as a function of AOD.
- 985 Figure 7. AEH error of (a) MITR, (b) WASO, and (c) COPO for the AOD difference of
986 0.1 as a function of reference AEH and AOD.
- 987 Figure 8. AEH error of (a) MITR, (b) WASO, and (c) COPO for the AOD difference of
988 0.1 as changing viewing geometries.
- 989 Figure 9. Same as Figure 7 except for SSA difference of 10%.
- 990 Figure 10. Same as Figure 7 except for particle size difference of 20%.
- 991 Figure 11. Same as Figure 7 except for surface albedo difference of 0.02.
- 992 Figure 12. Flowchart of the retrieval algorithm for AEH from OMI observation.
- 993 Figure 13. (a) MODIS RGB, (b) AOD, (c) FMF, and (d) AEH distribution from OMI
994 over East Asia, and (e) Backscattering Intensity at 532 nm from CALIOP observation
995 over Yellow Sea on March 31, 2007.
- 996 Figure 14. (a) MODIS RGB, (b) AOD, (c) FMF, and (d) AEH distribution from OMI
997 over East Asia, and (e) Backscattering Intensity at 532 nm from CALIOP observation
998 over coastal region of China on February 21, 2008.
- 999 Figure 15. Comparison of AEH from OMI with CALIOP with (a) AOD > 0.5, and (b)
1000 AOD > 1.0 for aerosol transport cases in 2007 and 2008 over East Asia.

1001

1002 **Tables**

1003 Table 1. The database of cross section used for DOAS fitting analysis.

Species	Temperature (K)	Reference
O ₃	223, 243, and 273	Bogumil <i>et al.</i> (2001)
NO ₂	220 and 294	Vandaele <i>et al.</i> (1998)
O ₄	298	Hermans <i>et al.</i> (1999)

1004

1005 Table 2. Dimensions of LUT for the clear sky comparison.

Variable name	No. of Entries	Entries
SZA	7	0, 10, 20, 30, 40, 50, 60 degrees
VZA	7	0, 10, 20, 30, 40, 50, 60 degrees
RAA	10	0, 20, 40, 60, 80, 100, 120, 140, 160, 180 degrees

1006 SZA : Solar zenith angle, VZA : Viewing zenith angle, RAA: Relative azimuth angle.

1007

1008 Table 3. Dimensions of simulation cases for the error analysis of the AEH retrieval.

Variable name	No. of Entries	Entries
SZA	7	0, 10, 20, 30, 40, 50, 60 degrees
VZA	7	0, 10, 20, 30, 40, 50, 60 degrees
RAA	10	0, 20, 40, 60, 80, 100, 120, 140, 160, 180 degrees
AOD	5	0.4, 1.0, 1.6, 2.5, 3.0
AEH	8	1.0, 1.2, 1.6, 2.0, 2.4, 3.0, 4.0, 5.0 km
Aerosol Model	3	MITR, WASO, COPO
Surface Albedo	1	0.10

1009 AOD: Aerosol Optical Depth, AEH : Aerosol Effective Height

1010

1011 Table 4. Absolute difference of O4I for changing surface albedo by 0.02.

	MITR	WASO	COPO
Maximum	81	85	76
Case [AOD,AEH]	[0.4,5.0]	[0.4,5.0]	[0.4,5.0]
Minimum	8	11	1
Case [AOD,AEH]	[3.0,1.0]	[3.0,1.0]	[3.0,1.0]
Mean±Standard Deviation	38±22	37±20	20±21

1012

1013

1014 Table 5. The error for AEH due to the change in aerosol vertical distribution.

Reference shape (half-width=1 km)	MITR (half-width=2 km)	WASO (half-width=2 km)	COPO (half-width=2 km)
Error for AEH [m]	1477±602	671±265	722±190

1015

1016

1017

1018 Table 6. Summary of error sources and total error budget for the AEH retrieval.

Error source	MITR	WASO	COPO
AOD (Δ AOD = 0.2)	387±740 m	105±131 m	218±358 m
SSA (10% change)	726±537 m	1047±194 m*	576±332 m
Surface Albedo ($\Delta\alpha = 0.02$)	438±762 m	199±241 m	154±274 m
Particle Size (20% change)	352±174 m	72±56 m	315±213 m
Atmospheric Gases		< 5 m	
Atmospheric Pressure** (Δ P = 3%)		3.4±0.1% (O ₄ SCD)	
Instrument (Shift : 0.02 nm)		<10 m	
Total Error	1276 m	846 m	739 m

1019 * Calculation results for the SSA decrease by 10%.

1020 ** For clear sky calculation.

1021

1022

1023 Table 7. Dimensions of LUT for the AEH algorithm using OMI.

Variable name	No. of Entries	Entries
SZA	7	0, 10, 20, 30, 40, 50, 60 degrees
VZA	7	0, 10, 20, 30, 40, 50, 60 degrees
RAA	10	0, 20, 40, 60, 80, 100, 120, 140, 160, 180 degrees
AOD	13	0.0, 0.2, 0.4, 0.6, 0.8, 1.0, 1.3, 1.6, 1.9, 2.2, 2.5, 3.0, 5.0
AEH	16	0.0, 1.0, 1.2, 1.4, 1.6, 1.8, 2.0, 2.2, 2.4, 2.6, 2.8, 3.0, 3.5, 4.0, 5.0, 10.0 km
Aerosol Model	3	Dust, Carbonaceous, Non-absorbing [Climatology over East Asia site of AERONET]

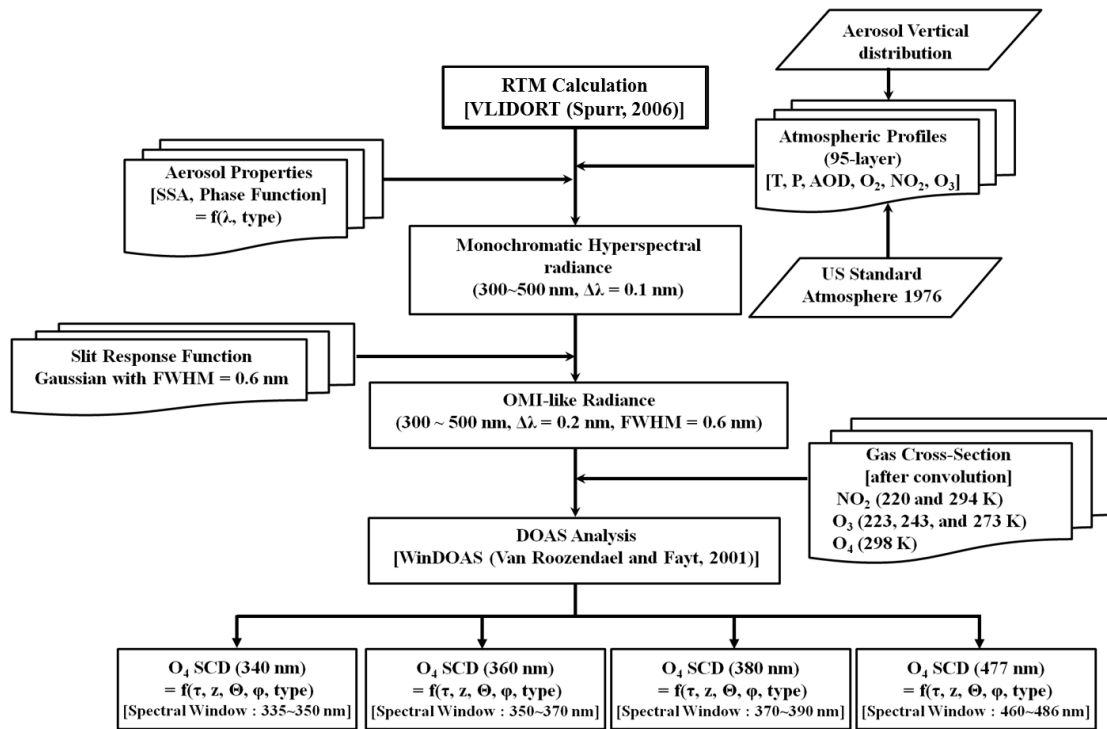
1024

1025 Table 8. List of aerosol transport cases and its period for comparison.

Case	Period
1	March, 28, 2007 - April, 2, 2007
2	May, 5, 2007 - May, 10, 2007
3	May, 25, 2007 - May, 26, 2007
4	February, 19, 2008 - February, 21, 2008
5	April, 3, 2008 - April, 5, 2008
6	May, 28, 2008 - May, 31, 2008
7	December, 4, 2008 - December, 7, 2008

1026

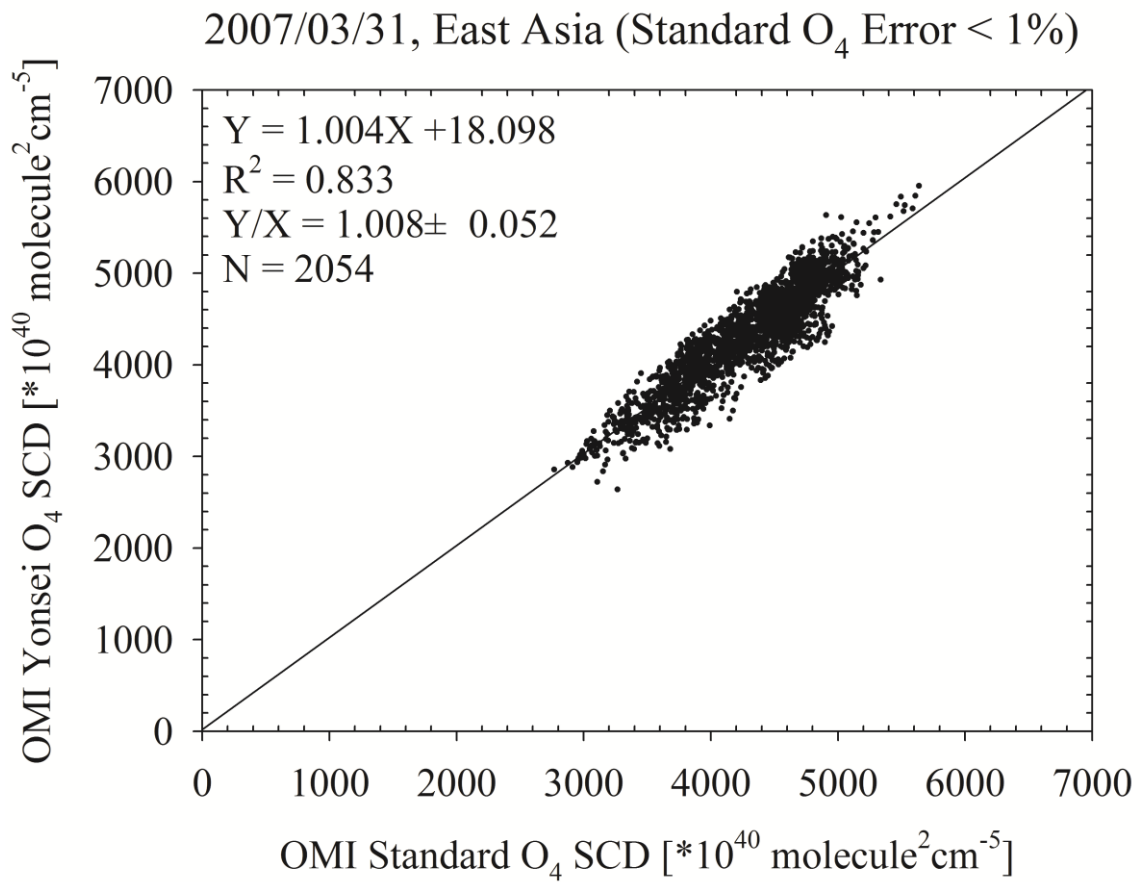
1027



1029

1030 Figure 1. Flowchart of the simulated O₄ SCD estimation.

1031



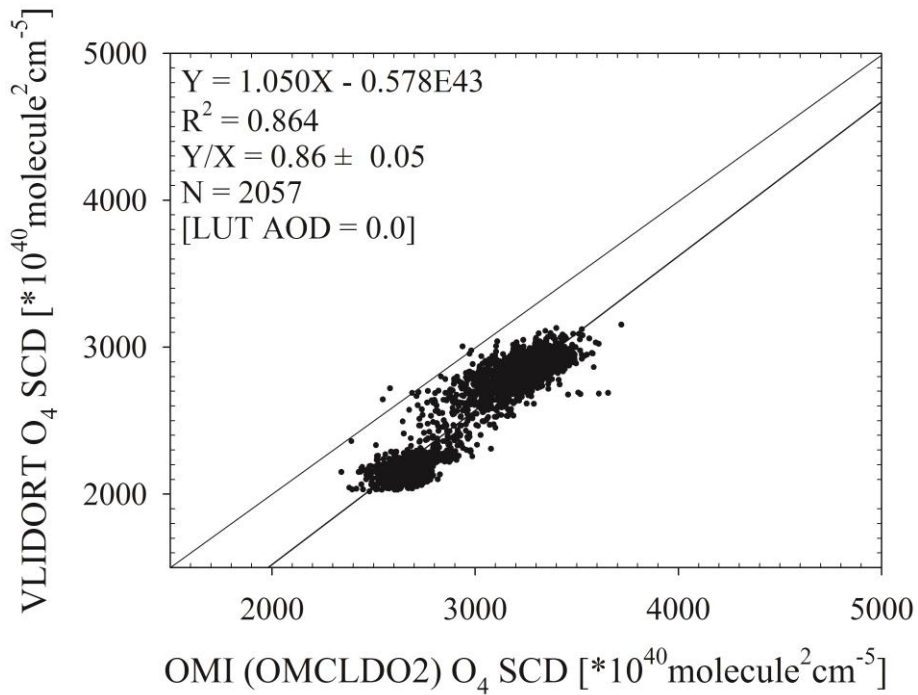
1032

1033 Figure 2. Comparison of O₄ SCD directly retrieved from OMI radiance with the OMI
 1034 standard product on March 31, 2007.

1035

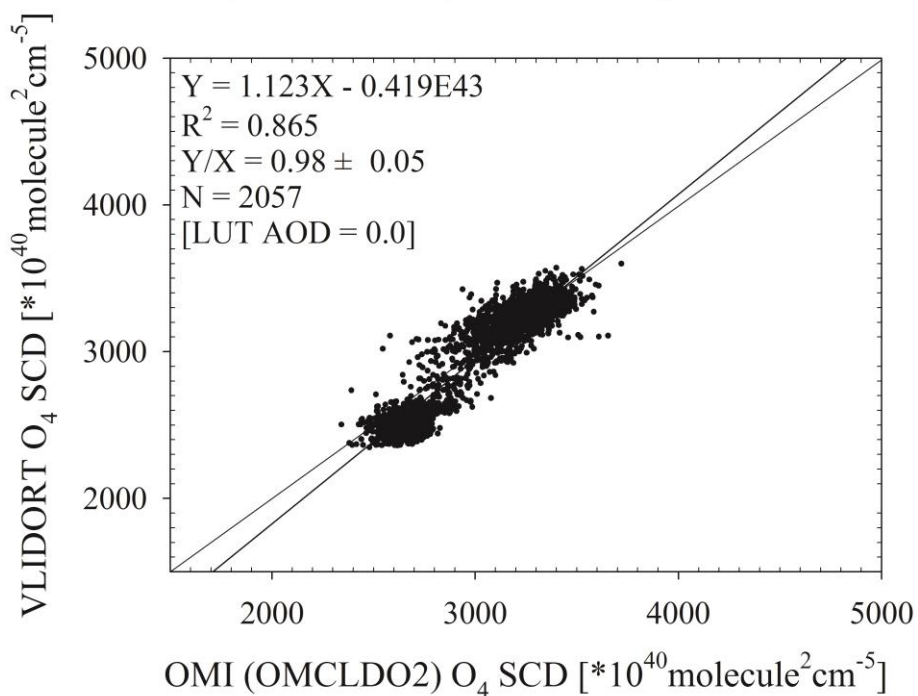
1036 (a)

Year 2005, Fit error <2%, Pacific Ocean, Cloud Fraction < 0.02



1037
1038 (b)

Year 2005, Fit error <2%, Pacific Ocean, Cloud Fraction < 0.02



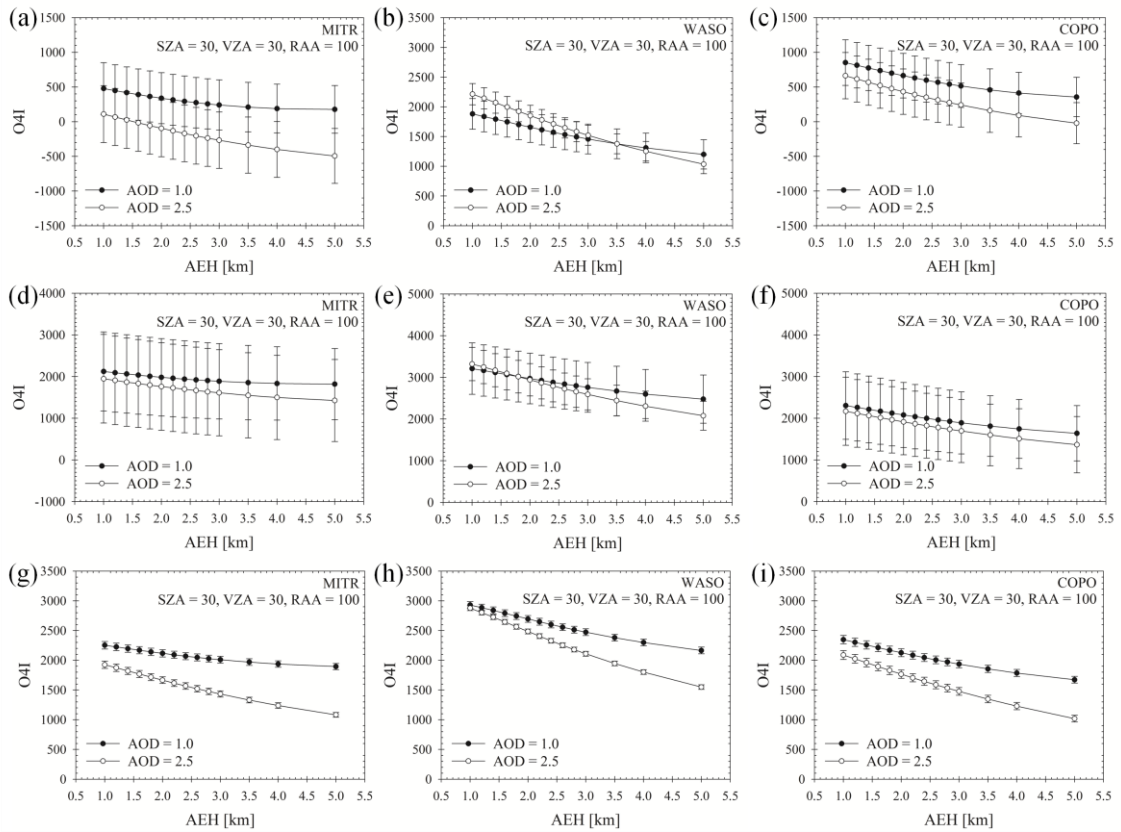
1039

1040 Figure 3. Comparison of the O₄ SCD at 477 nm between the OMI standard product and

1041

the calculated value from LUT (a) before and (b) after correction of LER.

1042



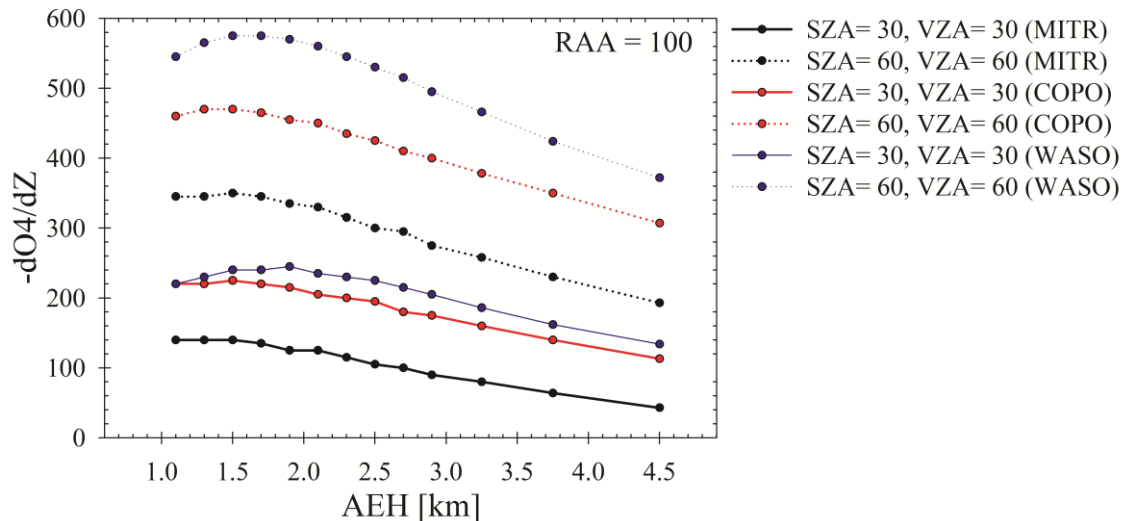
1043

1044

1045

1046

Figure 4. The O4I at 360 nm band for (a) MITR, (b) WASO, and (c) COPO, (d) at 380 nm band for MITR, (e) WASO, and (f) COPO, and (g) at 477 nm band for MITR, (h) WASO, and (i) COPO as a function of AEH.



1047

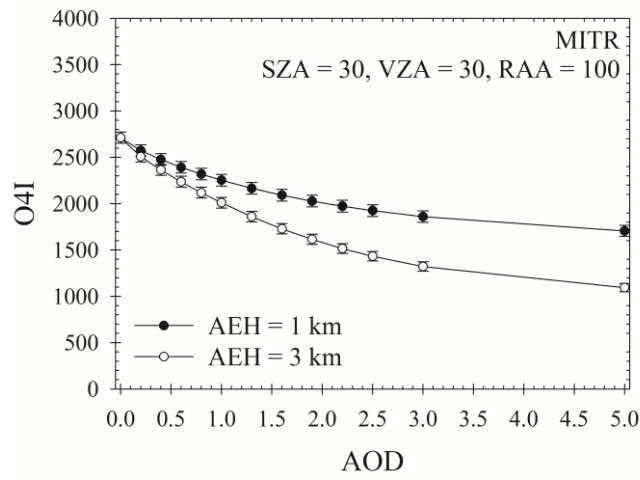
1048

1049

Figure 5. The AEH sensitivity to O4I ($-dO_4/dZ$) with changing observation geometries at 477 nm.

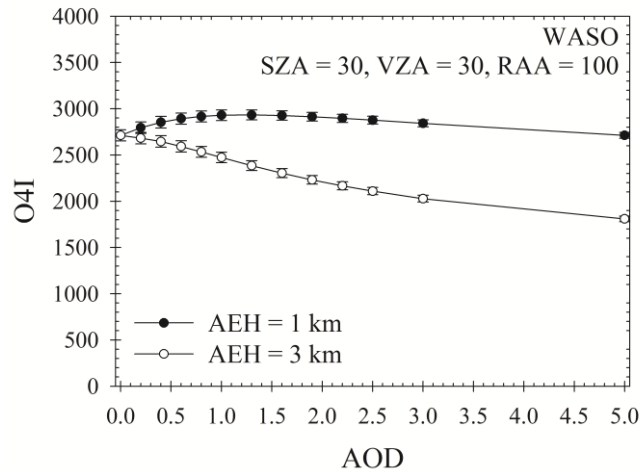
1050

(a)



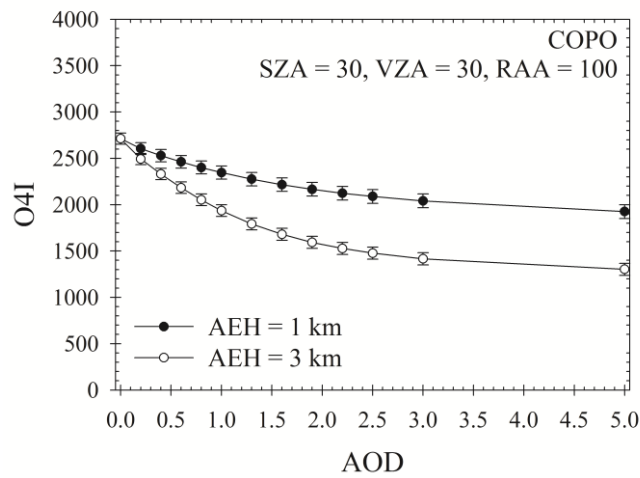
1051
1052

(b)



1053
1054

(c)



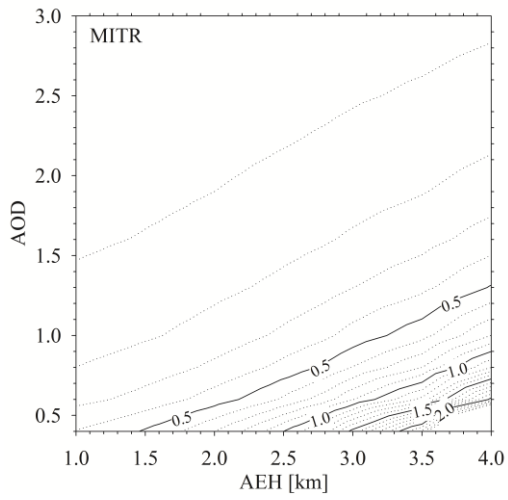
1055

1056

Figure 6. The O4I of (a) MITR, (b) WASO, and (c) COPO types as a function of AOD.

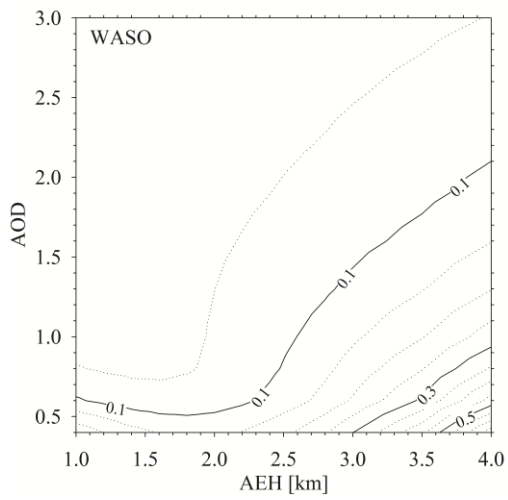
1057

1058 (a)



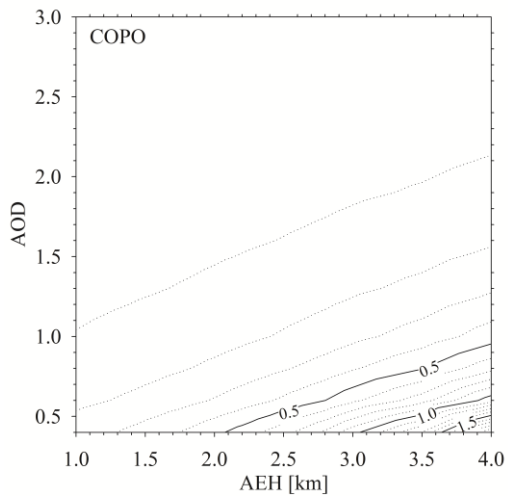
1059
1060

(b)



1061
1062

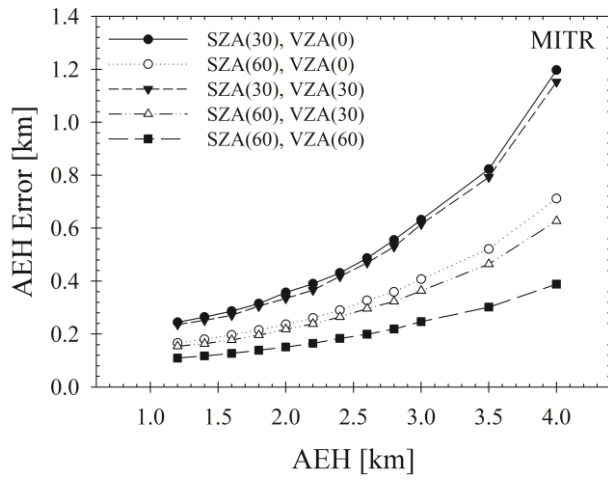
(c)



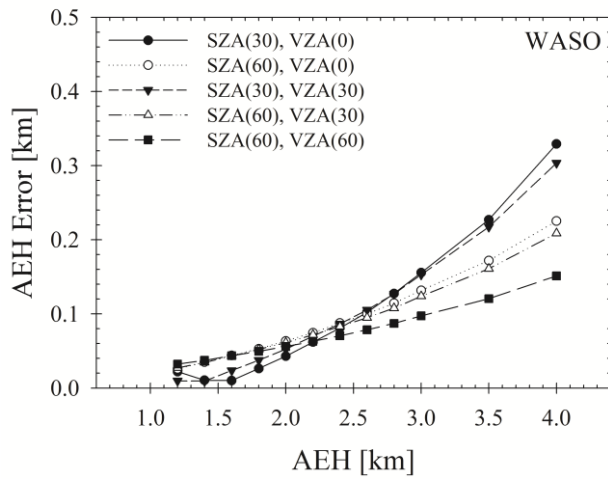
1063
1064
1065

Figure 7. AEH error of (a) MITR, (b) WASO, and (c) COPO for the AOD difference of 0.1 as a function of reference AEH and AOD.

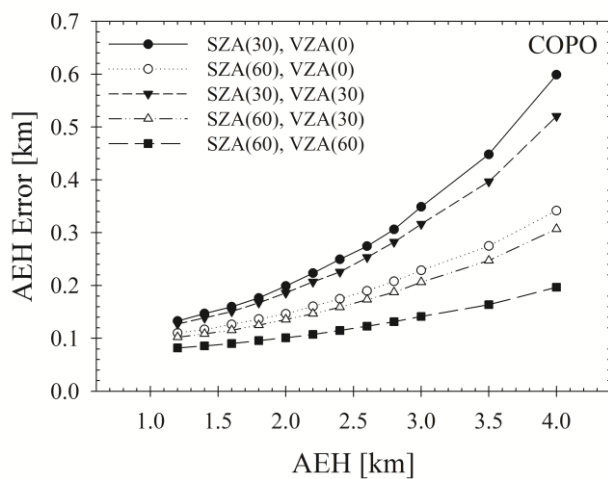
1066 (a)



1067
1068 (b)



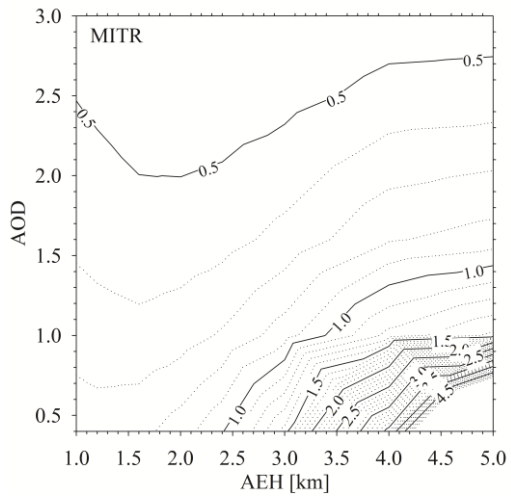
1069
1070 (c)



1071
1072
1073
1074

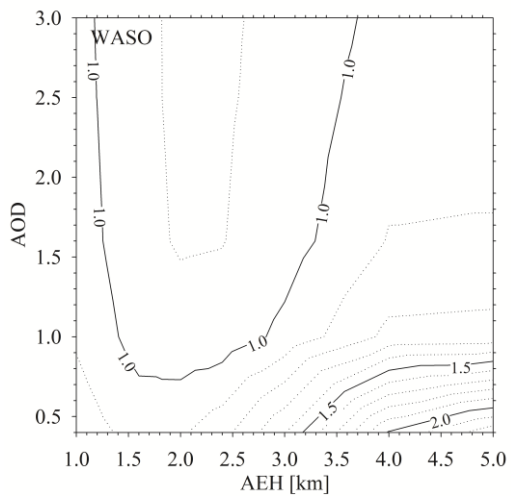
Figure 8. AEH error of (a) MITR, (b) WASO, and (c) COPO for the AOD difference of 0.1 as changing viewing geometries.

1075 (a)



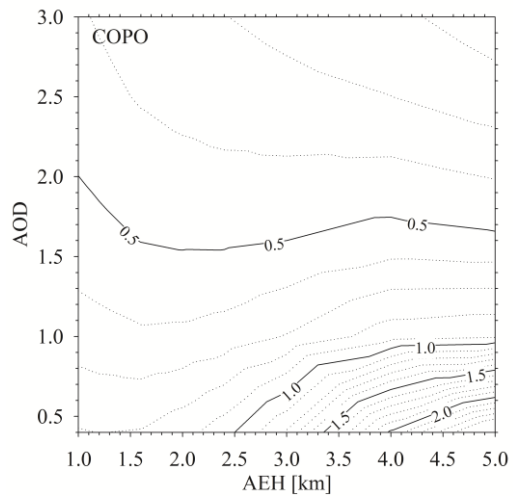
1076
1077

(b)



1078
1079

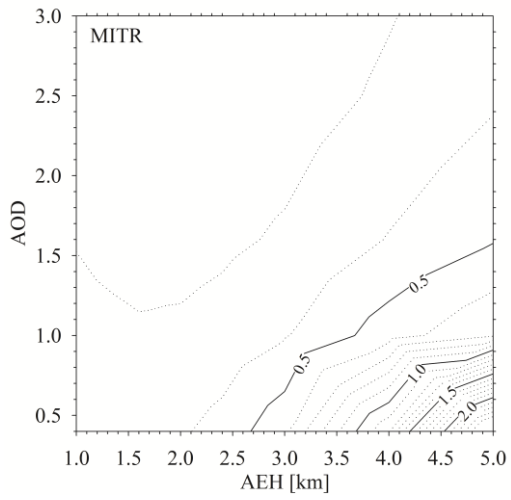
(c)



1080
1081

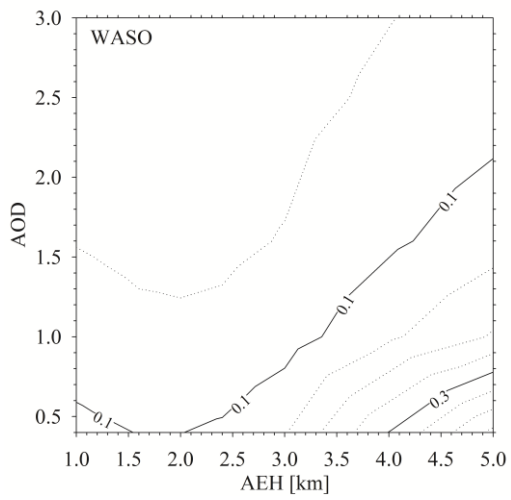
Figure 9. Same as Figure 7 except for SSA difference of 10%.

1082 (a)



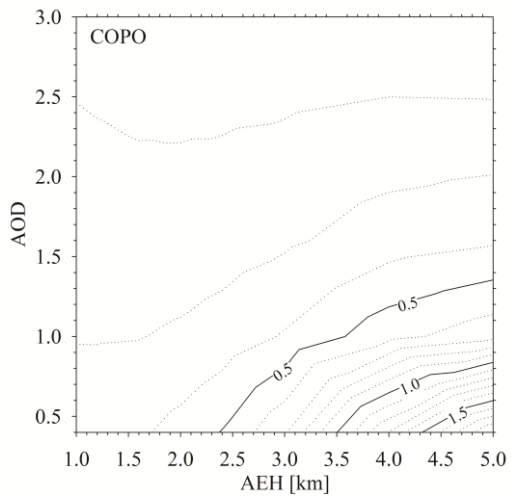
1083
1084

(b)



1085
1086

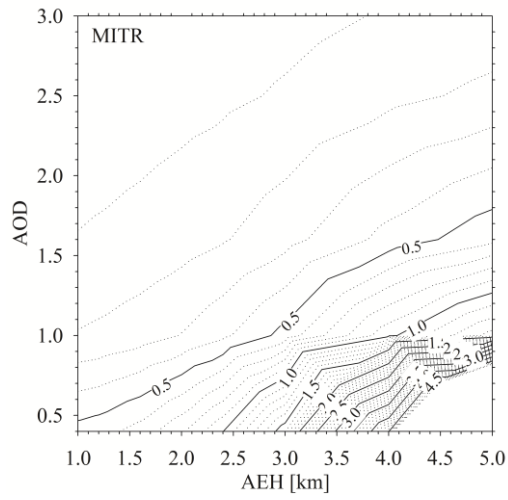
(c)



1087
1088

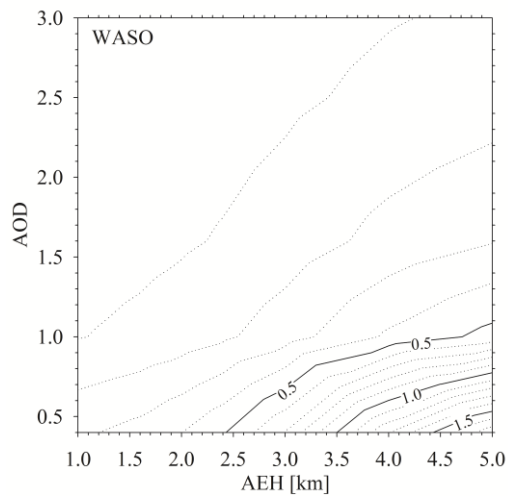
Figure 10. Same as Figure 7 except for particle size difference of 20%.

1089 (a)



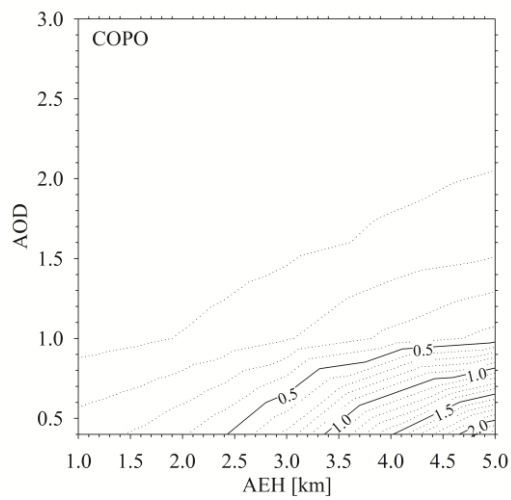
1090
1091

(b)



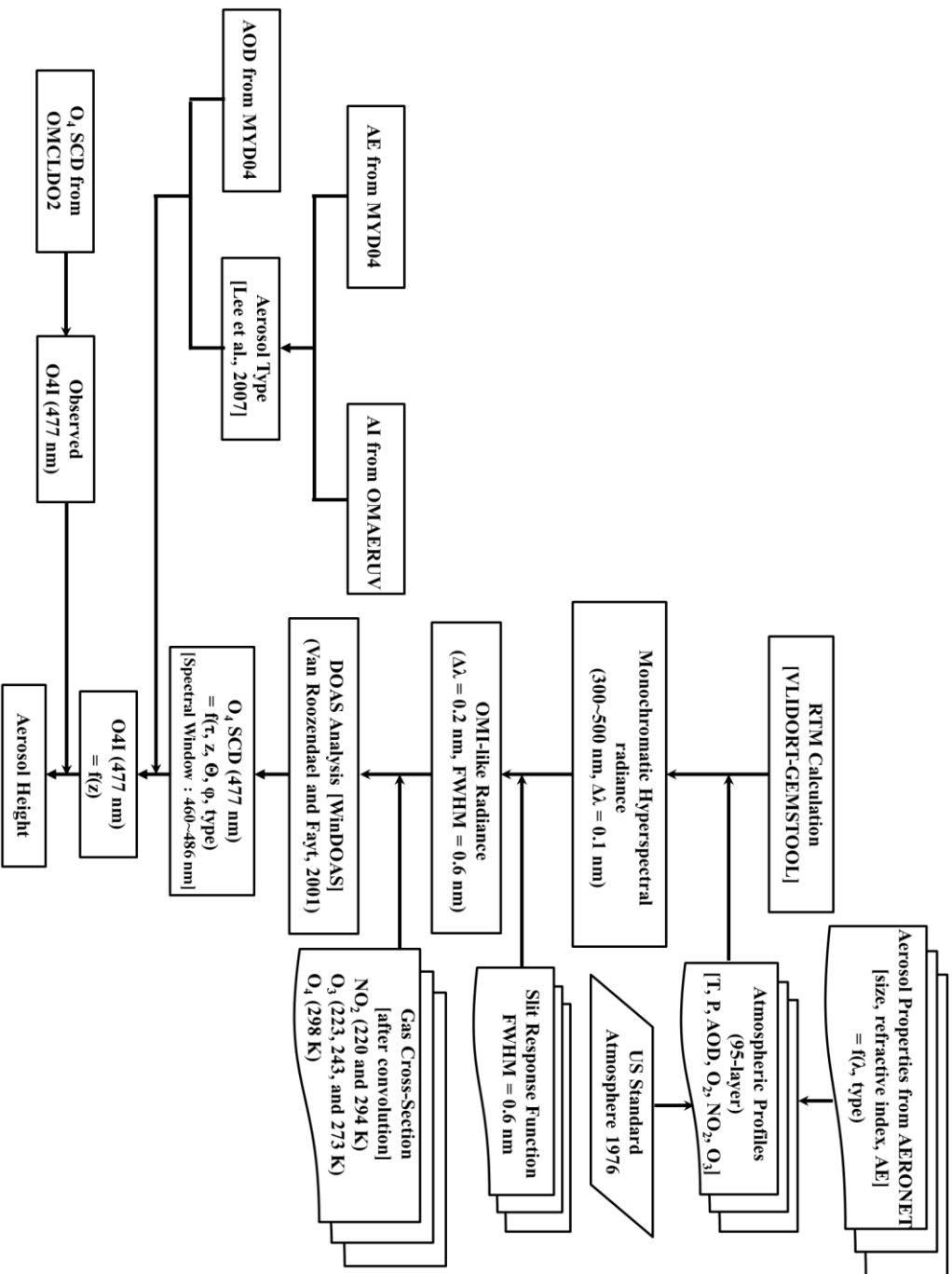
1092
1093

(c)



1094
1095

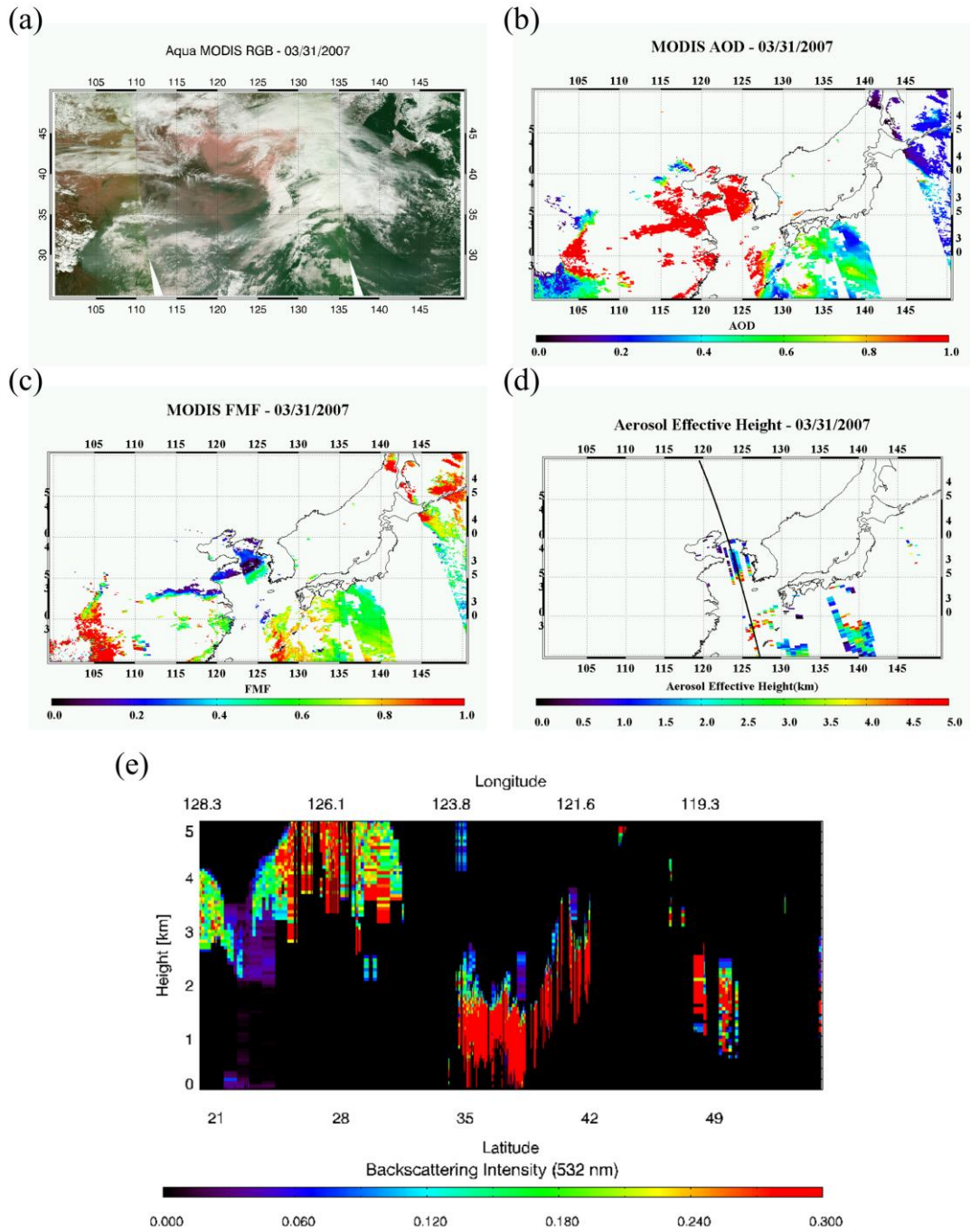
Figure 11. Same as Figure 7 except for surface albedo difference of 0.02.



1096

1097

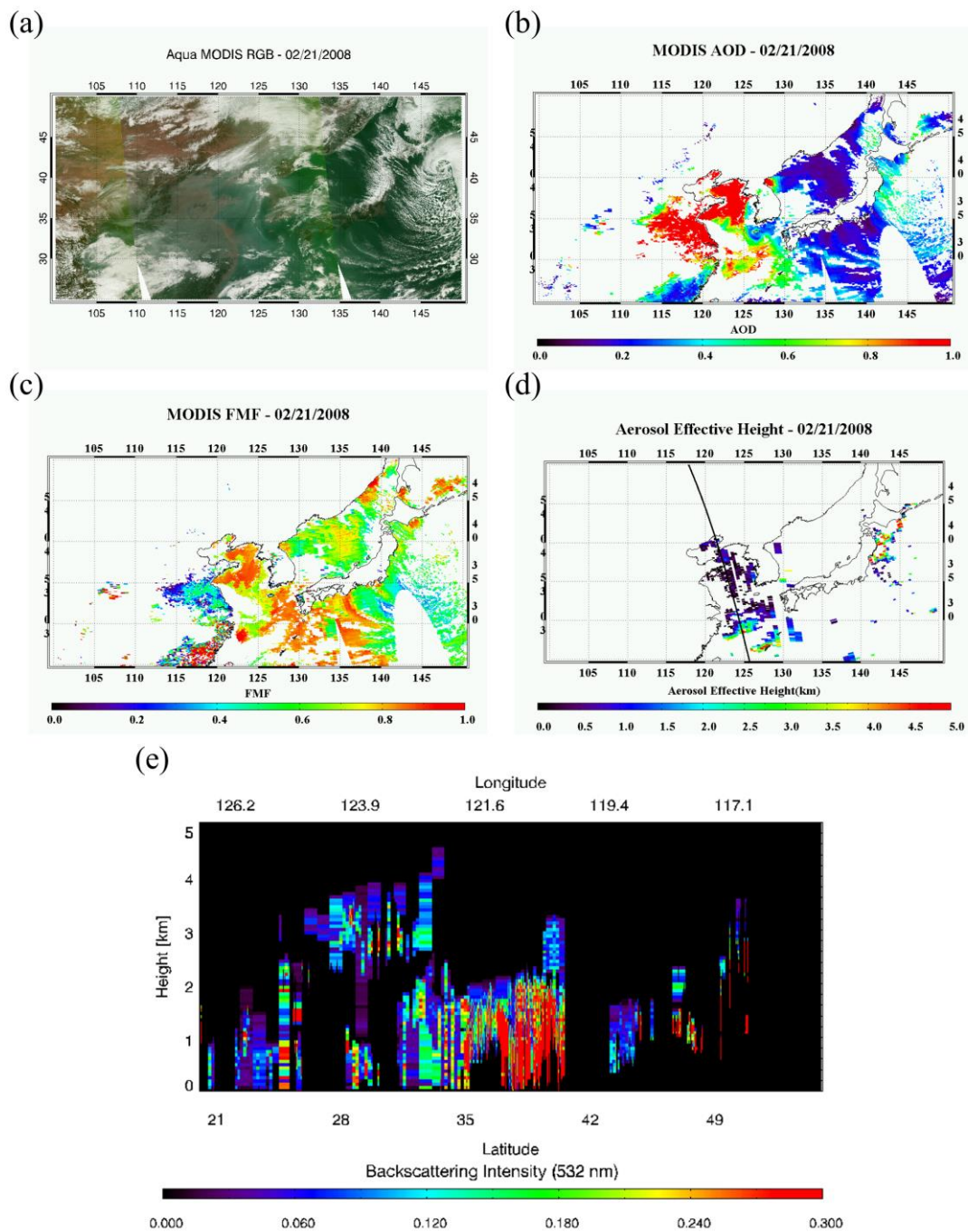
Figure 12. Flowchart of the retrieval algorithm for AEH from OMI observation.



1098

1099 Figure 13. (a) MODIS RGB, (b) AOD, (c) FMF, and (d) AEH distribution from OMI
 1100 over East Asia, and (e) Backscattering Intensity at 532 nm from CALIOP observation
 1101 over Yellow Sea on March 31, 2007.

1102

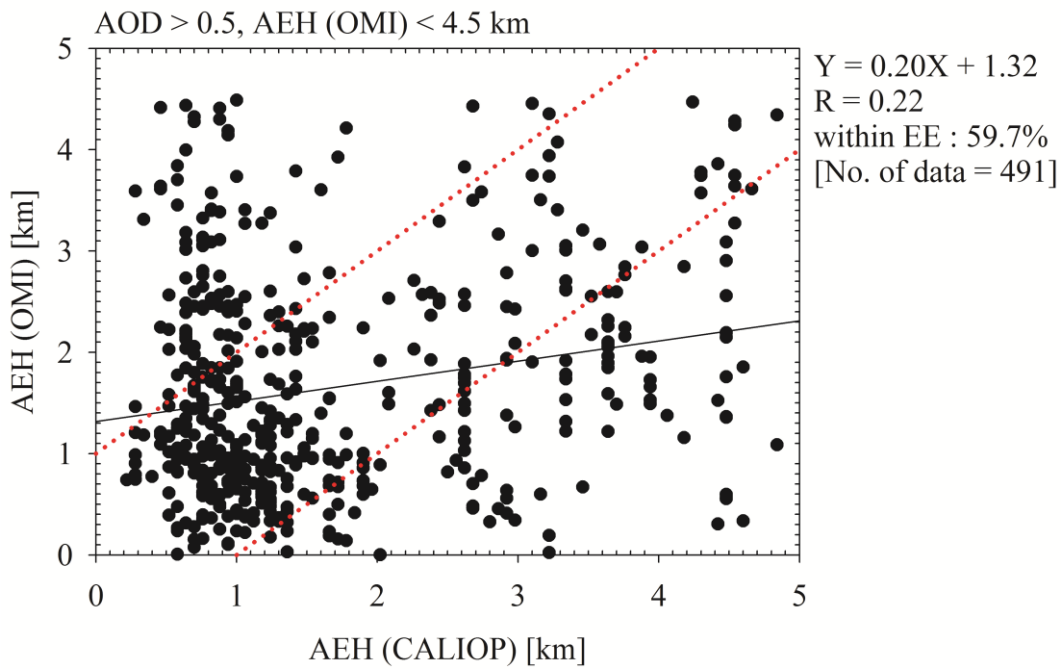


1103

1104 Figure 14. (a) MODIS RGB, (b) AOD, (c) FMF, and (d) AEH distribution from OMI
 1105 over East Asia, and (e) Backscattering Intensity at 532 nm from CALIOP observation
 1106 over coastal region of China on February 21, 2008.

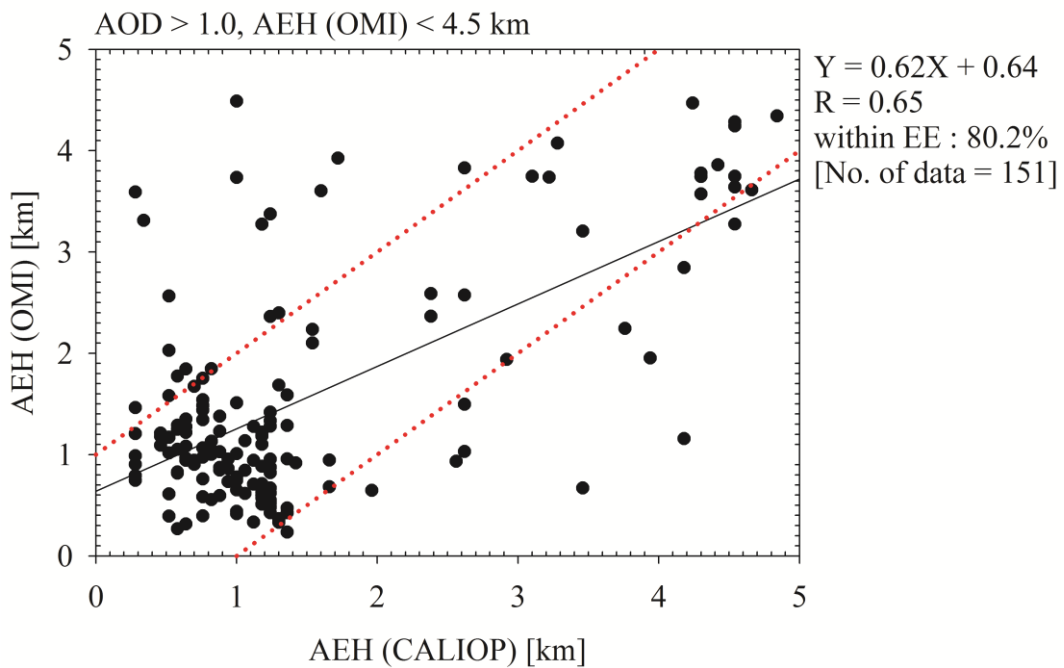
1107

1108 (a)



1109
1110

(b)



1111

1112 Figure 15. Comparison of AEH from OMI with CALIOP with (a) AOD > 0.5, and (b)

1113 AOD > 1.0 for aerosol transport cases in 2007 and 2008 over East Asia.

1114

1115

1116